Smart Materials in Manufacturing 5 (2027) 100148

Contents lists available at ScienceDirect

Smart Materials in Manufacturing

journal homepage: www.keaipublishing.com/en/journals/smart-materials-in-manufacturing

Research Paper

Excellent yield strength-to-Young's modulus ratio in crystallographic texture-controlled β-type Ti–42Nb alloy developed by laser powder bed fusion

Keitaro Miyasawa [a], Ryosuke Ozasa [a,b,*], Daisuke Egusa [c], Eiji Abe [c], Masakazu Tane [a,b], Kazuhisa Sato [d], Pan Wang [e], Takayoshi Nakano [a,b,**]

[a] Division of Materials and Manufacturing Science, Graduate School of Engineering, The University of Osaka, 2-1 Yamadaoka, Suita, Osaka, 565-0871, Japan
[b] 3DPTec Integrated Center, The University of Osaka, 2-1 Yamadaoka, Suita, Osaka, 565-0871, Japan
[c] Department of Materials Science and Engineering, University of Tokyo, Tokyo, 113-8656, Japan
[d] Research Center for Ultra-High Voltage Electron Microscopy, The University of Osaka, 7-1 Mihogaoka, Ibaraki, Osaka, 567-0047, Japan
[e] Singapore Institute of Manufacturing Technology (SIMTech), Agency for Science, Technology and Research (A*STAR), 5 Cleantech Loop, 636732, Republic of Singapore

ARTICLE INFO

Keywords:
Laser powder bed fusion
Metastable β-type Ti alloy
Crystallographic texture
Microstructure
Mechanical property

ABSTRACT

This study developed a crystallographic texture-controlled Ti–42Nb alloy via laser powder bed fusion (L-PBF), characterized its microstructures, and evaluated their contributions to mechanical properties through numerical calculations. By employing different scanning strategies in L-PBF, three types of strong textures with <001>, <011>, and <111> orientations along the building direction were successfully developed. Scanning electron microscopy and transmission electron microscopy analyses revealed the formation of columnar dendrites with slight elemental segregation and the absence of dislocation cells. Moreover, this study clarified the formation of small amounts of nanosized precipitates comprising ω and α″ phases. The texture-controlled specimens exhibited pronounced anisotropy in Young's modulus depending on crystal orientation, similar to that observed in single crystals, with a 2.1-fold difference between the <001>- and <111>-oriented specimens. Notably, the results clarified the contribution of the nanosized ω phase to a significant increase in yield strength without affecting Young's modulus. The <001>-oriented specimen exhibited reasonable yield strength (635.3 MPa) and plastic elongation (13.6%) while maintaining a low Young's modulus (40.9 GPa), demonstrating that the combination of texture control and nanosized ω phase formation is crucial for regulating the mechanical properties of metastable β-type Ti alloys. The yield strength-to-Young's modulus ratio of this alloy (15.5×10^{-3}) is one of the highest values among Ti alloys. These findings provide valuable insights into microstructural control using L-PBF and highlight the impact of microstructures on both elastic and plastic mechanical behavior.

1. Introduction

Metal additive manufacturing (AM) has attracted significant attention for fabricating three-dimensional (3D) shapes [1–4]. Among AM techniques, laser powder bed fusion (L-PBF) has been increasingly employed to fabricate metallic components with complex geometries, particularly for biomedical applications [5–7]. In addition, owing to the characteristic melting and solidification behavior in the L-PBF process, L-PBF enables control of microstructural features, including crystallographic texture in materials with various crystal structures [8–11], elemental distributions [12,13], and the formation of cellular structures [14] and fine compounds [15]. In recent years, studies have reported that L-PBF-derived microstructures affect yield strength [16], high-cycle fatigue properties [17], high-temperature strength [18], and corrosion

Peer review under the responsibility of Editorial Board of Smart Materials in Manufacturing
* Corresponding author. Division of Materials and Manufacturing Science, Graduate School of Engineering, The University of Osaka, 2-1 Yamadaoka, Suita, Osaka, 565-0871, Japan.
** Corresponding author. Division of Materials and Manufacturing Science, Graduate School of Engineering, The University of Osaka, 2-1 Yamadaoka, Suita, Osaka, 565-0871, Japan.
E-mail addresses: ozasa@mat.eng.osaka-u.ac.jp (R. Ozasa), nakano@mat.eng.osaka-u.ac.jp (T. Nakano).

https://doi.org/10.1016/j.smmf.2026.100148
Received 1 April 2026; Received in revised form 1 July 2026; Accepted 13 July 2026

resistance [19]. However, despite the anticipated strong influence of crystallographic texture on mechanical properties, this relationship remains poorly understood. This is partly because precise control of crystallographic texture remains challenging using currently available L-PBF approaches.

To clarify the relationship between crystallographic texture and mechanical properties, this study focused on Ti–Nb alloys, which are among the metastable β-type Ti alloys. Metastable β-type Ti alloys exhibit pronounced elastic anisotropy [20]. The degree of elastic anisotropy depends on the average valence electron concentration (e/a, where e is the number of valence electrons and a is the total number of atoms) and increases as the e/a value approaches 4. For example, a single crystal of the Ti–15Mo–5Zr–3Al (wt.%) alloy, with $e/a = 4.1$, exhibits an elastic modulus of ~120 GPa along the <111> direction and a minimum value of ~44 GPa along the <001> direction [21]. In particular, Ti–Nb alloys with the e/a of 4.26–4.30 are known to exhibit high mechanical anisotropy and an exceptionally low Young's modulus owing to unique anelastic relaxation caused by reversible atomic shuffling events [22]. Therefore, the Ti–42Nb (wt.%) alloy ($e/a = 4.27$) provides an ideal model for investigating the effects of crystallographic texture on mechanical properties.

Ti–Nb alloys with low e/a values close to 4.0 have low stability of the β phase with a body-centered cubic (BCC) structure and have been reported to form athermal ω, martensitic α″, and isothermal ω phases within the β matrix during fabrication processes [23,24]. The ω phase exhibits higher hardness and Young's modulus but poor ductility [23], whereas the α″ phase exhibits comparable or even superior mechanical properties [24]. Furthermore, Ti–26Nb (at.%; ~Ti–41Nb (wt.%), $e/a = 4.26$) and Ti–27Nb (at.%; ~Ti–42Nb (wt.%), $e/a = 4.27$) alloys exhibit a stress-induced α″ martensitic transformation during deformation [25–27]. Although the α″ martensitic transformation can provide unique deformation behavior through transformation-induced plasticity effects [25] and superelasticity [26], it may potentially lead to an intrinsic reduction in yield strength. These previous studies were conducted using arc-melted Ti–Nb alloys, in which the oxygen concentration was maintained at a low level. Because oxygen suppresses formation of the α″ phase by lowering the martensitic transformation temperature [28], the influence of the α″ martensitic transformation could be pronounced in arc-melted materials. Therefore, to accurately understand the effects of microstructure on the mechanical properties of Ti–42Nb, the effects of both the ω and α″ phases should also be considered.

To date, several studies have investigated metastable β-type Ti alloys fabricated by L-PBF. Mantri et al. reported that an as-built Ti–10V–2Fe–3Al (wt.%) alloy formed the ω phase, which suppressed deformation twinning typically observed in forged materials [29]. Schaal et al. demonstrated that an as-built Ti–22Zr–7Nb–2Sn (at.%) alloy underwent stress-induced α″ martensitic transformation during deformation [30]. These studies indicate that metastable phases formed during the L-PBF process can significantly influence the deformation behavior and mechanical properties of metastable β-type Ti alloys.

For Ti–Nb alloys, previous studies have reported that L-PBF-fabricated Ti–41Nb (wt.%) forms the ω phase but not the α″ phase [31]. In contrast, the presence and role of ω and α″ phases in as-built Ti–42Nb alloys have not been clarified [32–34]. Furthermore, the stress–strain curves reported for L-PBF-fabricated Ti–42Nb alloys exhibit neither the characteristic two-stage yielding associated with stress-induced α″ martensitic transformation nor serrated flow related to twinning [32,33]. Although these features were not specifically discussed in the original studies, their absence suggests that stress-induced α″ martensitic transformation and twinning may be suppressed under L-PBF conditions. Thus, the influence of microstructural features on the mechanical properties of L-PBF-fabricated Ti–Nb alloys has not yet been sufficiently discussed.

The aim of this study is to develop texture-controlled Ti–42Nb alloys using different L-PBF scanning strategies, characterize their microstructures and mechanical properties, and evaluate the contributions of microstructural factors to mechanical properties through calculations. Particular focus is placed on elucidating the respective contributions of texture-induced modulus variation and metastable-phase strengthening to the yield strength-to-Young's modulus ratio (σ_y/E), which is an important indicator for load-bearing biomedical implants, and on identifying microstructural design strategies for maximizing σ_y/E. The present findings provide comprehensive insights into the relationship between microstructure, including crystal orientation and the ω/α″ phases, and mechanical properties, including Young's modulus and yield strength, in Ti–42Nb.

2. Materials and methods

2.1. Specimen fabrication

Pre-alloyed Ti–42Nb feedstock powder was procured from Taniobis GmbH (Germany). The powder exhibited a spherical shape with $D_{50} = 40.0$ μm, as measured using a Mastersizer 3000 (Malvern Panalytical, UK). The L-PBF process was conducted using an EOS M290 system (EOS, Germany), in which the laser power P, scanning speed v, hatch spacing d, and stacking thickness t were set to 240–360 W, 600–1200 mm· s^{-1}, 0.08 mm, and 0.06 mm, respectively. An energy density (ED) in the range of 41.7–125 J ·mm^{-3} was applied, as calculated using Eq. (1) [10].

$$ED = P / vdt \ (\mathrm{J{\cdot}mm^{-3}}) \quad (1)$$

Specimens with dimensions of 5 mm × 5 mm × 10 mm for microstructural observation and 5 mm × 5 mm × 25 mm for tensile testing were fabricated under an Ar atmosphere, with the oxygen concentration in the chamber maintained below 1000 ppm. This study employed three types of scanning strategies to develop crystallographic textures with different crystal orientations based on a previous study [9]. Bidirectional scanning only along the x-axis (±X_SS), bidirectional scanning along the x- and y-axes with 90° rotation between layers (±XY_SS), and unidirectional scanning with 120° rotation between layers (+120°_SS) produced <001>-, <011>-, and <111>-oriented textures, respectively. The laser scanning directions and patterns for ±X_SS, ±XY_SS, and +120°_SS are illustrated in Fig. 1. The building direction and the direction parallel to the front of the machine were defined as the z- and x-axes (0° direction), respectively, whereas the y-axis (90° direction) was defined as perpendicular to the x- and z-axes, following the ISO/-ASTM 52900 standard terminology.

Inductively coupled plasma atomic emission spectroscopy (ICP-AES; ICPV-1017, Shimadzu, Japan) was used to measure the composition of the feedstock powder and the L-PBF-fabricated specimen for Nb detection. The inert gas fusion method (TCH600, LECO, USA) was used to detect O and N.

2.2. Microstructural characterization

The mirror-polished cross-section of the yz-plane, perpendicular to the x-axis of the specimens, was observed using an optical microscope (OM; BX60, Olympus, Japan). The relative density was evaluated from the OM images using ImageJ software (NIH, USA). The area fraction of the defects (f_{defect} (%)) was measured using threshold segmentation, and the relative density was calculated by subtracting f_{defect} from 100.

Crystallographic texture was observed using field-emission scanning electron microscopy (FE-SEM; JIB-4610F, JEOL, Japan) equipped with electron backscatter diffraction (EBSD; NordlysMax 3, Oxford Instruments, UK), with a step size of 2 μm and an accelerating voltage of 20 kV. Inverse pole figure (IPF), pole figure, and grain boundary (GB) maps were obtained using AZtec (Oxford Instruments, UK) and processed using Channel 5 (Oxford Instruments, UK). Low-angle grain boundaries (LAGBs, $2° \leq \theta < 15°$) and high-angle grain boundaries

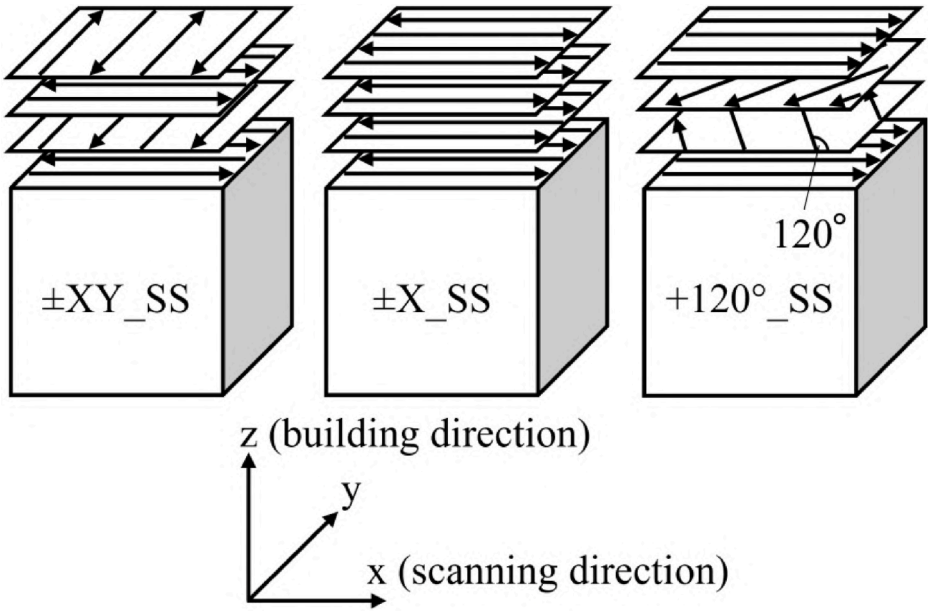

Fig. 1. Schematic of each scanning strategy employed in this study. (a) ±XY_SS, (b) ±X_SS, and (c) +120°_SS.

(HAGBs, $\theta \geq 15°$) were classified on the GB map, where θ is the crystal misorientation angle between neighboring pixels. The grain boundary spacings (d_y and d_z) were determined from the GB maps using the line intercept method along the y- and z-axes. The obtained values are expressed as the mean ± standard deviation.

To quantitatively characterize the evolved texture, the degrees of orientation (p) of <001>, <011>, and <111> along the z-axis were calculated based on the Euler angles obtained by EBSD as

$$p_{<hkl>} = \langle \cos^2 \alpha_{<hkl>} \rangle, \tag{2}$$

where $\alpha_{<hkl>}$ represents the angular deviation of <001>, <011>, or <111> from the z-axis, as analyzed using Euler angles at each analysis point on the IPF map. The average value of $\cos^2 \alpha_{<hkl>}$ is defined as the degree of crystal orientation for $< hkl >$, denoted as $p_{<hkl>}$ [35]. Considering the multiplicity of crystal planes, the degrees of orientation for randomly oriented <001>, <011>, and <111> were 0.74, 0.84, and 0.80, respectively. A perfect orientation leads to $p = 1$ [35]. Chemically etched specimens were used to observe the solidified microstructures.

Transmission electron microscopy (TEM; JEM 2010HC and JEM-3010, JEOL, Japan) operated at an acceleration voltage of 200 kV and 300 kV, and aberration-corrected scanning transmission electron microscopy (STEM; JEM ARM200F, JEOL, Japan) operated at an acceleration voltage of 200 kV with a convergence half angle of 22 mrad, were used for high-magnification observations. The specimens were prepared using ion milling (PIPS model 691, Gatan, USA), a twin-jet electropolishing system (Tenupol-3, Struers, Denmark), or a focused ion beam (FIB) instrument (Scios 2 DualBeam, Thermo Fisher Scientific, USA).

2.3. Tensile test

The test specimens were extracted from the center of the L-PBF-fabricated samples, with the gauge direction corresponding to the z-axis (Fig. S1(a)). The sample surfaces were polished to a #2000-grit finish. The geometry and dimensions of the tensile specimens were determined with reference to a previous study [36], and the detailed specimen dimensions are illustrated in Fig. S1(b). The longitudinal and transverse directions of the specimens corresponded to the z- and x-axes, respectively. Tensile tests were conducted using a universal testing machine (AGX-V, Shimadzu, Japan) at a strain rate of $1.67 \times 10^{-4}\,s^{-1}$. The testing environment was set at room temperature under atmospheric pressure. Strain throughout the test was determined from the crosshead displacement. Although the crosshead displacement reasonably represents the specimen strain in the plastic deformation region, it may include not only the elastic strain of the specimen but also the elastic deformation of the testing machine and grips in the elastic region. Therefore, the elastic strain of the specimen was evaluated using strain gauges (KFGS-1N-120-C1-11 L1M2R, KYOWA, Japan) directly attached to both sides of the gauge section of the specimens. Young's modulus was then determined from the slope of the stress–strain curve between 20% and 80% of the yield strength.

2.4. Statistical analysis

In this study, quantitative results are expressed as mean ± standard deviation. The significance of the mechanical properties (n = 3) was tested using one-way analysis of variance (ANOVA), followed by Tukey's post hoc test. A p-value < 0.05 was considered statistically significant.

2.5. Numerical simulation of thermal diffusion

A finite element thermal diffusion simulation (COMSOL Multiphysics 6.3, COMSOL Inc., Sweden), which has been established for various types of alloys [10,11,37,38], was conducted to evaluate the temperature conditions during solidification. For the simulation, the energy distribution of the heat source was assumed to follow a Gaussian distribution [39], and the 3D energy distribution was expressed as a function of radius r and depth z. The expression is given as

$$Q = \frac{4AP}{\pi R^2 H} \exp\left(-\frac{2r^2}{R^2}\right)\left[1 - \frac{z}{H}\right] \quad (0 < z < H), \tag{3}$$

where Q is the amount of heat per unit volume, P is the laser power, R is the radius of the laser spot, r is the distance from the powder bed surface to the center of the laser spot, A is the laser absorption rate, H is the penetration depth, and z is the depth. Additionally, this study used a surface energy flux absorption model in which the Gaussian heat flux, attenuated with penetration depth, was deposited on the top surface [40]. Although convection in the melt pool was not calculated in this model, the simplification had a relatively small effect on the melt pool geometry and temperature field [41]. The heat transfer equation of the fluid was obtained from a domain simulation using Eq. (4) [11].

$$\rho C_p \frac{\partial T}{\partial t} + \nabla \cdot \boldsymbol{q} = Q, \tag{4}$$

where ρ is the absolute density, C_p is the specific heat capacity, T is the temperature, t is the time, $\boldsymbol{q}$ is the heat flux, and Q is the heat generation rate per unit volume. The heat flux resulting from heat conduction was computed according to Fourier's law [11].

$$\boldsymbol{q} = -k\nabla T, \tag{5}$$

where k is the thermal conductivity. The boundary conditions on the outer surface of the model [11] were defined as

$$-\boldsymbol{n}\cdot\boldsymbol{q} = q_0 = h(T_{ext} - T), \tag{6}$$

where $\boldsymbol{n}$ is the normal vector of the surface through which heat flows; h is the heat transfer coefficient, which was set to 76 $W{\cdot}m^{-2}{\cdot}K^{-1}$; and T_{ext} is the external temperature at which the model contacts the environment (powder bed). T_{ext} was set to T_0.

The physical properties of the Ti–42Nb alloy (Table 1), calculated using JMatPro® (Sente Software, UK), were used in the simulations. The dimensions of the finite element model were 5 mm (width) × 5 mm (depth) × 10 mm (height). Single-laser scanning with a laser path length of 5 mm was simulated. The validity of the simulation model was verified by demonstrating that the error between the simulated and experimentally measured melt pool dimensions was less than 2%, as shown in Table S1. This simulation is based on a simplified single-track model and serves as a supplementary analysis; it does not fully capture the complex thermal histories of the actual multi-track and multi-layer L-PBF process. The thermal gradient (G) and solidification rate (R) at the solid–liquid interface in the melt pool were analyzed at the midpoint along the laser scan track. The cooling rate during solidification was estimated as the product of G and R at each pixel, and these values were averaged.

3. Results

3.1. Characterization of Ti–42Nb alloy fabricated by L-PBF

Changes in relative density as a function of the process parameters are represented in Fig. 2. OM images and the corresponding relative densities of specimens fabricated using ± XY_SS (Fig. 2(a)), ±X_SS (Fig. 2(b)), and +120°_SS (Fig. 2(c)) were observed. The relative density varied depending on ED. The density was maximized at an ED of 75 $J{\cdot}mm^{-3}$ ($P = 360$ W and $v = 1000$ $mm{\cdot}s^{-1}$); nearly full density (> 99.98%) was achieved at this ED regardless of the scanning strategy (Fig. 2(d)). Under high ED conditions (> 83.3 $J{\cdot}mm^{-3}$), keyhole-type pores formed owing to excessive melting, leading to a decrease in the density to below 99%. Table 2 lists the chemical compositions of the feedstock powder and the L-PBF-fabricated Ti–42Nb alloy. The dense specimen fabricated using the ±XY_SS at $ED = 75.0$ $J{\cdot}mm^{-3}$ was used as a representative sample to exclude contamination from gases contained in pores. By comparison, ~300 and ~160 ppm of O and N were introduced during the L-PBF process, respectively.

Table 1
Physical and thermophysical parameters in the thermal diffusion simulation of Ti–42Nb alloy.

Physical parameter	Value
β transus temperature, $T_{\alpha\beta}$ (K)	920.1
Solidus temperature, T_s (K)	1961.7
Liquidus temperature, T_l (K)	2124.7
Density, ρ ($kg{\cdot}m^{-3}$)	5639.9
Specific heat capacity of solid ($T > T_S$), C_s ($J{\cdot}(kg{\cdot}K)^{-1}$)	720.1
Specific heat capacity of liquid ($T > T_l$), C_l ($J{\cdot}(kg{\cdot}K)^{-1}$)	934.3
Latent heat, H ($kJ{\cdot}kg^{-1}$)	288.3

3.2. Crystallographic texture formation depending on scanning strategies and process parameters

Variations in crystallographic texture as a function of the process parameters for each scanning strategy are illustrated in Figs. 3–5. In the ±XY_SS (Fig. 3(a)), most fabricated specimens exhibited a preferential <100> alignment along the x-, y-, and z-axes, and the condition with $ED = 75.0$ $J{\cdot}mm^{-3}$ demonstrated the highest degree of <100> orientation along the z-axis (Fig. 3(b)–3(d)). In the ±X_SS (Fig. 4(a)), most specimens formed a preferential <100> alignment along the x-axis, whereas the orientation along the z-axis varied with the process parameters. Under conditions with $ED = 75.0$ $J{\cdot}mm^{-3}$, crystals with two predominant orientations were observed. One was oriented with {011} planes along the y- and z-axes and {001} planes along the x-axis. The other exhibited {001} orientation along the x-, y-, and z-axes. Conversely, the <100> alignment was prominently along the x-, y-, and z-axes under conditions with $ED = 125$ $J{\cdot}mm^{-3}$. These trends were consistent with the quantitative analysis results (Fig. 4(b)–4(d)). In the +120°_SS (Fig. 5), intermediate ED conditions resulted in a strong texture with preferential <111> alignment along the z-axis, whereas conditions with $ED = 125$ $J{\cdot}mm^{-3}$ or $ED \leq 62.5$ $J{\cdot}mm^{-3}$ led to the formation of polycrystalline structures. Accordingly, strong textures with distinct crystal orientations, in which <001>, <011>, and <111> were primarily aligned along the z-axis, were successfully formed by employing different scanning strategies. In the subsequent analyses, specimens developed at $ED = 75$ $J{\cdot}mm^{-3}$ (laser power of 360 W and scanning speed of 1000 $mm{\cdot}s^{-1}$) were used as representative samples for all scanning strategies.

The GB maps and distributions of crystal misorientation angles are illustrated in Fig. 6, and the characteristics of the GBs are summarized in Table 3. The specimens exhibited columnar crystal grains elongated along the z-axis, regardless of the scanning strategy (Fig. 6(a)–6(c)); however, the spacing between grain boundaries, namely the grain boundary density, differed among specimens (Table 3). The distributions revealed that both LAGBs and HAGBs were formed in comparable fractions in the ±X_SS specimen (Fig. 6(e)), whereas LAGBs were predominantly formed in the ±XY_SS (Fig. 6(d)) and +120°_SS (Fig. 6(f)) specimens, corresponding to the trend in the degree of crystal orientation. Consequently, HAGBs were rarely observed in the strongly textured ± XY_SS specimens. These results suggest that both grain boundary distribution and crystallographic texture can be controlled by adjusting the scanning strategy.

3.3. Observation of solidified microstructures and dislocations in the ±XY_SS specimen

In this study, solidified microstructures and metastable phases were formed in a specimen fabricated using the ±XY_SS. Observations of the yz-plane using SEM in backscattered electron (BSE) imaging mode revealed that columnar dendrites were elongated along the z-axis at the center of the melt pool, whereas they were elongated normal to the z-axis on both sides of the pool (Fig. 7(a)). A high-magnification image showed that primary dendrite arm spacing (PDAS: λ) varied depending on the position within the melt pool (Fig. 7(b)). Specifically, λ was 1.04 μm near the melt pool boundary and 0.71 μm at the center of the melt pool, as measured along line 1 and line 2, respectively.

Moreover, elemental distribution was observed using STEM-EDS (Fig. 7(c)). The line scan profile (along the orange line) revealed that the Nb concentration fluctuated by ~1–2% between the dendritic and inter-dendritic regions. Thus, the contrast observed in the SEM–BSE image (Fig. 7(b)) was attributed to differences in elemental distribution. Bright-field TEM observation revealed that organized dislocation cells were not formed and that dislocations were sparsely distributed within grains in the Ti–42Nb alloy (Fig. 7(d)).

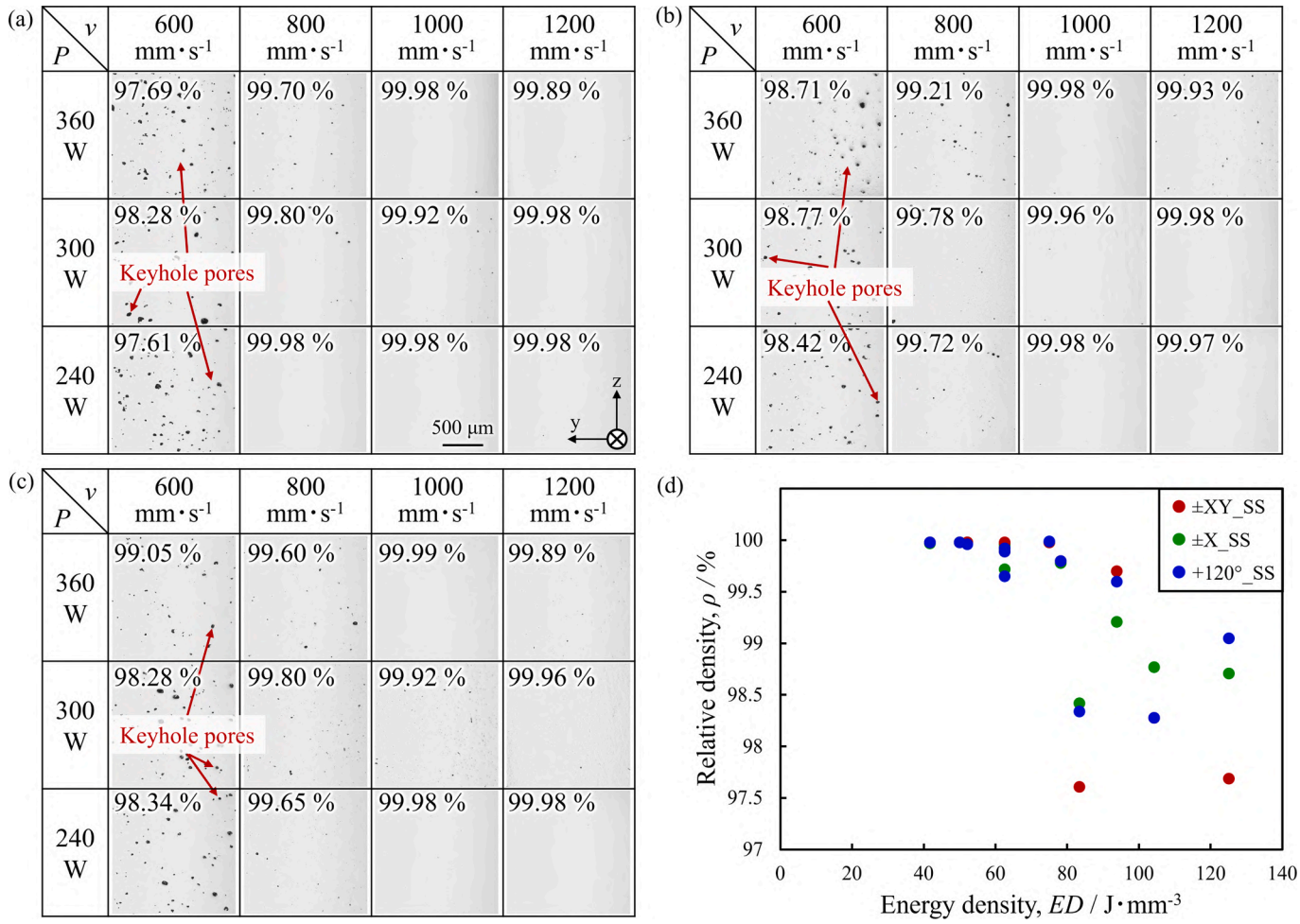

Fig. 2. Density of Ti-42Nb alloys fabricated at different conditions. OM micrographs for the yz-plane and the corresponding density of the alloy developed via (a) ±XY_SS, (b) ±X_SS, and (c) +120°_SS strategies. (d) Relationship between relative density and energy density.

Table 2
Composition of raw powder and the L-PBF-fabricated specimen.

Material	Ti (wt.%)	Nb (wt.%)	O (wt.%)	N (wt.%)
Powder	Bal.	41.8	0.20	0.016
L-PBF-fabricated	Bal.	41.5	0.23	0.032

3.4. Observation of nanosized precipitates in the ±XY_SS specimen

To investigate precipitates formed in the L-PBF-fabricated Ti–42Nb alloy, TEM and STEM observations were conducted using the ±XY_SS specimen as a representative sample (Fig. 8). The diffraction pattern along the [1$\bar{1}$0] zone axis (Fig. 8(a)) and the intensity profile taken along the line from 000_β to 112_β (Fig. 8(b)) revealed that ω and α″ phases were formed together with the β phase. The dark-field images of the ω_1 phase (Fig. 8(c)) and α″ phase (Fig. S2(b)) revealed that fine ω and α″ precipitates were dispersed in the β matrix. Additionally, the fast Fourier transform (FFT) pattern constructed from the HAADF-STEM image showed the presence of α″, ω_1, and ω_2 phases (Fig. 8(d)). Consistent with previous studies [42,43], both the ω and α″ phases exhibited specific orientation relationships with the β matrix, as described in Eqs. (7) and (8).

$$\{111\}_\beta // (0001)_\omega, <1\bar{1}0>_\beta // <11\bar{2}0>_\omega \quad (7)$$

$$\{110\}_\beta // \{001\}_{\alpha''}, <111>_\beta // <110>_{\alpha''} \quad (8)$$

These orientation relationships are schematically illustrated in Fig. 8 (f). Analysis using the inverse FFT (IFFT) image (Fig. 8(e)) revealed that the particle diameters (d_i) of the α″ and ω phases were ~3 nm. The volume fraction (f_i) and interparticle spacing (l_i) were calculated using Eqs. (9)–(11) [44].

$$f_i = \frac{4}{3}\pi\left(\frac{d_i}{2}\right)^3 n_v \quad (9)$$

$$l_i = \frac{1}{\sqrt{2 d_i n_v}} \quad (10)$$

$$n_v = \frac{n_s}{t} \times v \quad (11)$$

The areal density, volume density, and number of variants in each precipitated phase are denoted as n_s, n_v, and v, respectively. The thickness of the TEM specimen (t) used in this study was ~30 nm, as measured by STEM-EELS analysis. The ω and α″ phases contained four [45] and six [46] variants, respectively. The particles of each phase were characterized through observations and calculations (Table 4), and their sizes and volume fractions were comparable to those previously reported for Ti–xFe–xCo–1Mo (at.%) and Ti–10V–2Fe–3Al (wt.%) alloys fabricated via L-PBF [29,47]. Therefore, the L-PBF-fabricated Ti–42Nb alloy exhibited a microstructure consisting of crystallographic texture, columnar dendrites without organized dislocation cells, and fine precipitates of the ω and α″ phases.

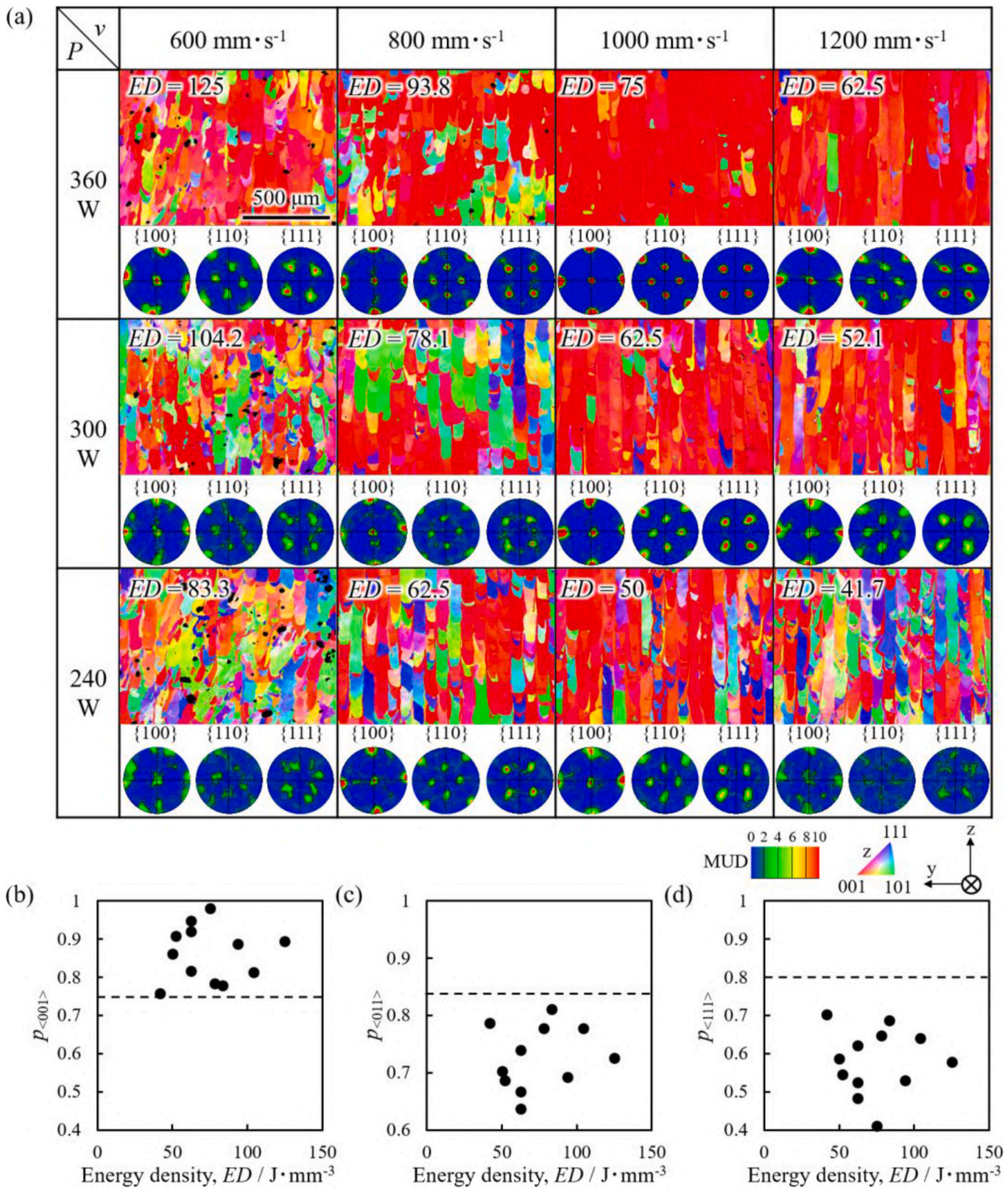

Fig. 3. Variations in crystallographic texture depending on process parameters of specimens developed via the ± XY_SS. (a) IPF maps projected along the z-axis and pole figures for {100}, {110}, and {111} observed along the yz-plane. Energy density (*ED* (J·mm^{-3})) is represented. The IPF maps and pole figures share the common coordinate system indicated at the bottom of (a). Relationship between energy density and degrees of orientation for (b) <001>, (c) <011>, and (d) <111> along the z-axis. Dashed lines indicate the value of random orientations.

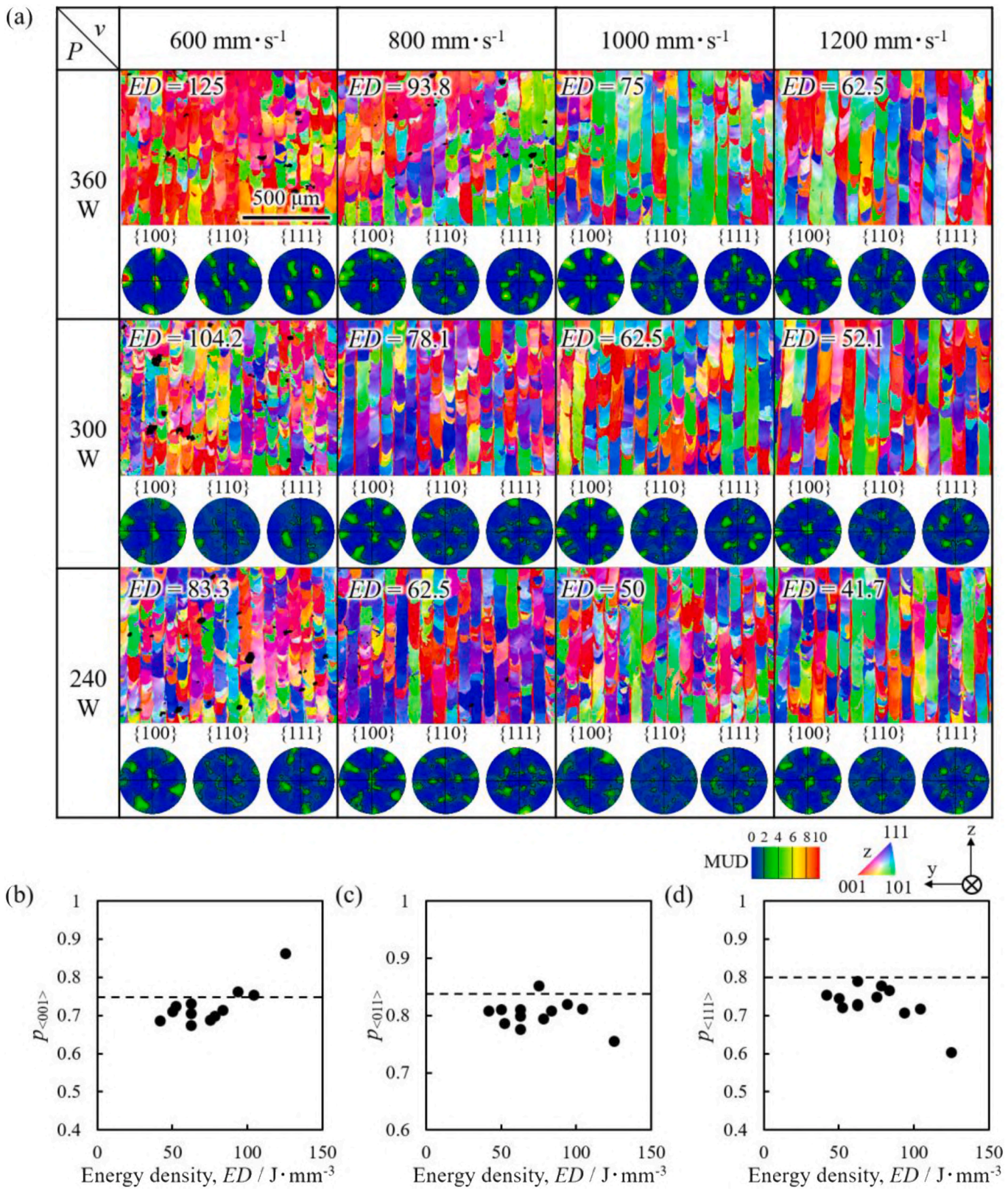

Fig. 4. Variations in crystallographic texture depending on the process parameters of specimens developed via the ± X_SS. (a) IPF maps projected along the z-axis and pole figures for {100}, {110}, and {111} observed along the yz-plane. Energy density (*ED* (J·mm^{-3})) is represented. The IPF maps and pole figures share the common coordinate system indicated at the bottom of (a). Relationship between energy density and degrees of orientation for (b) <001>, (c) <011>, and (d) <111> along the z-axis. Dashed lines indicate the value of random orientations.

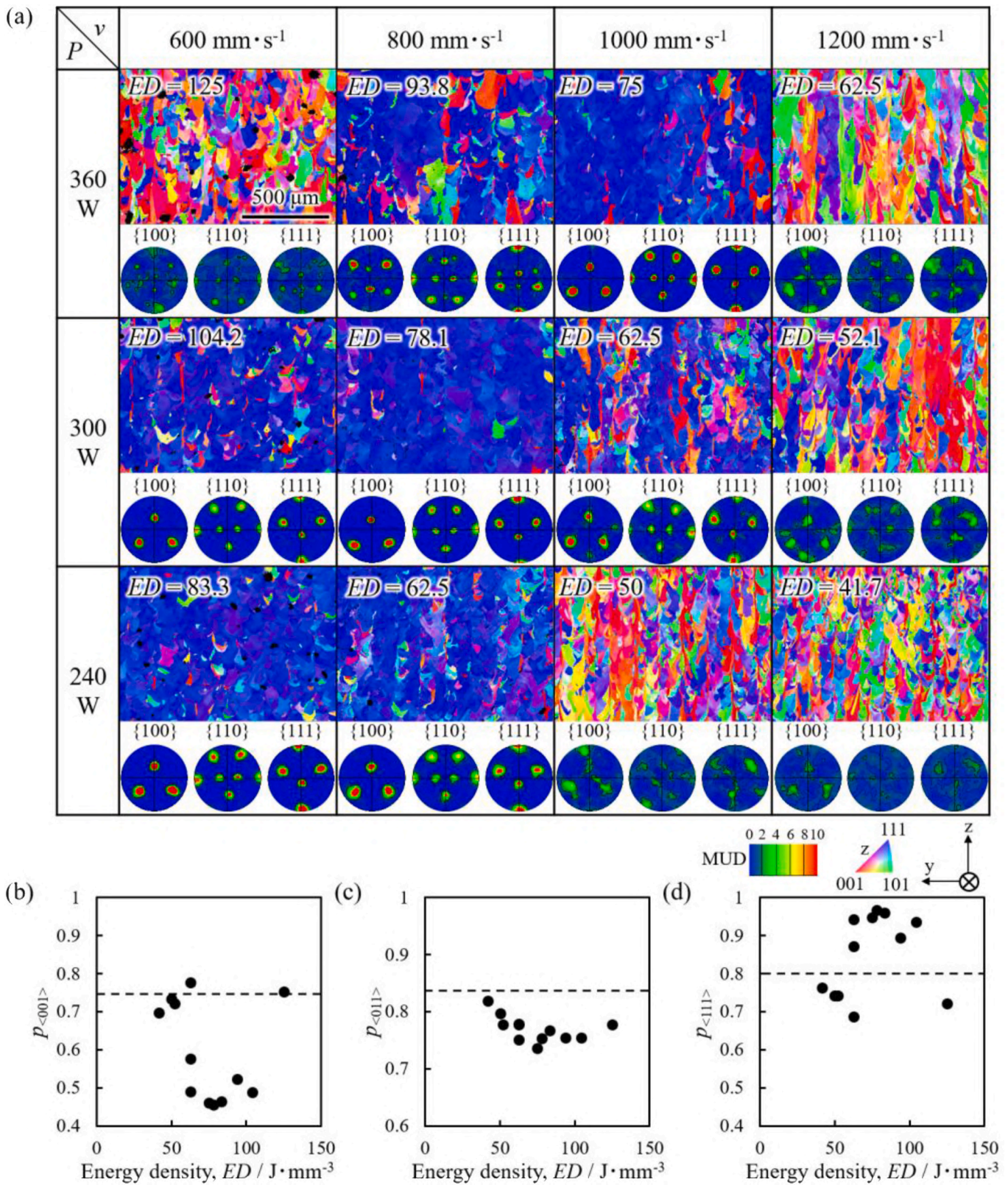

Fig. 5. Variations in crystallographic texture depending on the process parameters of specimens developed via the +120°_SS. (a) IPF maps projected along the z-axis and pole figures for {100}, {110}, and {111} observed along the yz-plane. Energy density (*ED* (J·mm^{-3})) is represented. The IPF maps and pole figures share the common coordinate system indicated at the bottom of (a). Relationship between energy density and degrees of orientation for (b) <001>, (c) <011>, and (d) <111> along the z-axis. Dashed lines indicate the value of random orientations.

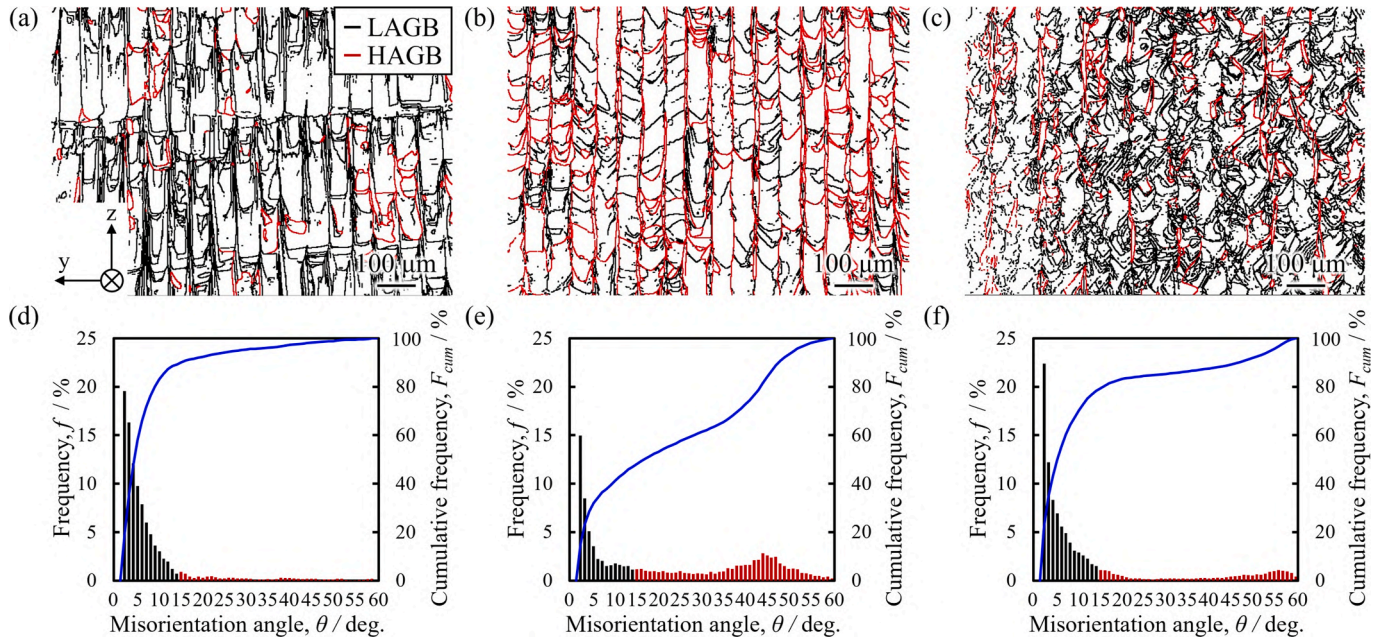

Fig. 6. Grain boundary (GB) distributions. GB maps and the distributions of crystallographic misorientation angle in (a, d) ±XY_SS, (b, e) ±X_SS, and (c, f) +120°_SS samples. LAGB ($2° \leq \theta < 15°$) and HAGB ($\theta \geq 15°$) were classified according to the crystal misorientation angle (θ) between neighboring pixels.

Table 3
Grain boundary spacing (LAGB and HAGB) and fractions of LAGB and HAGB in each specimen.

Material	Grain boundary spacing along y-axis, d_y (μm)	Grain boundary spacing along z-axis, d_z (μm)	Fraction of LAGB, f_{LAGB} (%)	Fraction of HAGB, f_{HAGB} (%)
±XY_SS	17.3 ± 1.7	70.0 ± 7.0	89.2	10.8
±X_SS	20.3 ± 1.3	63.9 ± 16.5	53.0	47.0
+120°_SS	19.7 ± 1.3	34.0 ± 6.6	78.3	21.7

3.5. Prediction of thermal diffusion behavior

To predict the geometry of the solidified microstructures formed during solidification, the thermal diffusion conditions in the melt pool were analyzed by focusing on the thermal gradient (G) and solidification rate (R) at the solid–liquid interface under laser irradiation conditions of $P = 360$ W and $v = 1000$ mm·s^{-1} (Fig. 9). The geometry of the simulated melt pool is shown in Fig. 9(a), while Fig. 9(b) shows the thermal diffusion conditions at each position in the melt pool plotted on a G–R map along with Hunt's columnar-to-equiaxed transition (CET) criterion for the Ti–6Al–4V (wt.%) alloy [48]. Most data points exceeded the CET criterion for predicting the formation of columnar dendrites. The average cooling rate within the melt pool, estimated as the product of G and R, is 6.6×10^6 K·s^{-1} in this study, which is significantly higher than that of conventional casting processes (~10^3 K·s^{-1}) [49,50].

3.6. Mechanical properties measured by tensile test

The mechanical properties of each specimen were evaluated by tensile testing, with the tensile direction corresponding to the z-axis in the coordinate system shown in EBSD results (Fig. 3(a), 4(a) and 5(a)). The initial parts of the true stress–strain curves and Young's modulus values are shown in Fig. 10(a) and (b), respectively. The <001>-oriented ± XY_SS specimen and the <111>-oriented +120°_SS specimen exhibited the lowest (40.9 GPa) and highest (84.8 GPa) Young's modulus values, respectively, whereas the ±X_SS specimen with a preferential <011> orientation exhibited an intermediate value (63.4 GPa). A comparison of the crystal-orientation dependence of Young's modulus between a Ti–40Nb single crystal and the present Ti–42Nb alloy is presented in Fig. 10(c). The Young's modulus of the Ti–40Nb single crystal was calculated using elastic stiffness constants reported in the literature [51]. The Young's moduli of the L-PBF-fabricated specimens varied similarly to those of the Ti–40Nb single crystal. Thus, by controlling crystal orientation via L-PBF, a pronounced elastic anisotropy of up to 2.1 times was achieved when comparing the ±XY_SS and +120°_SS specimens.

The true stress–plastic strain curves and work-hardening rates are shown in Fig. 10(d) and (e), respectively. At the oxygen and nitrogen concentrations used in the present study (Table 2), the characteristic two-stage yielding behavior associated with stress-induced α″ martensitic transformation was not observed during deformation (Fig. 10(a) and (d)), suggesting that the deformation behavior was primarily governed by dislocation slip rather than stress-induced α″ martensitic transformation. The analyzed values of yield strength (represented as bar graphs) and plastic strain (represented as plots) are shown in Fig. 10(f). The yield strength showed a significant variation depending on crystal orientation, with values in the order of +120°_SS > ±X_SS > ±XY_SS. These variations in yield stress are discussed in Section 4.1. No significant difference in ductility was observed.

In β-type Ti alloys, strain softening often occurs after yielding because dislocation slip tends to localize through the formation of slip bands [52]. However, the plastic deformation behavior of the L-PBF-fabricated specimens differed markedly depending on crystal orientation (Fig. 10(e)). After yielding, the XY_SS specimen exhibited stress softening, whereas the ±X_SS and +120°_SS specimens exhibited slight strain hardening. Furthermore, the ±X_SS specimen maintained a relatively stable flow stress, whereas the +120°_SS specimen underwent immediate softening. This study primarily focused on differences in Young's modulus and yield strength. The mechanism underlying the differences in plastic deformation behavior will be clarified in future studies.

4. Discussion

In this study, the texture and crystal orientation of the Ti–42Nb alloy were controlled by applying different scanning strategies during L-PBF. Moreover, this study revealed the formation of a small amount of fine ω

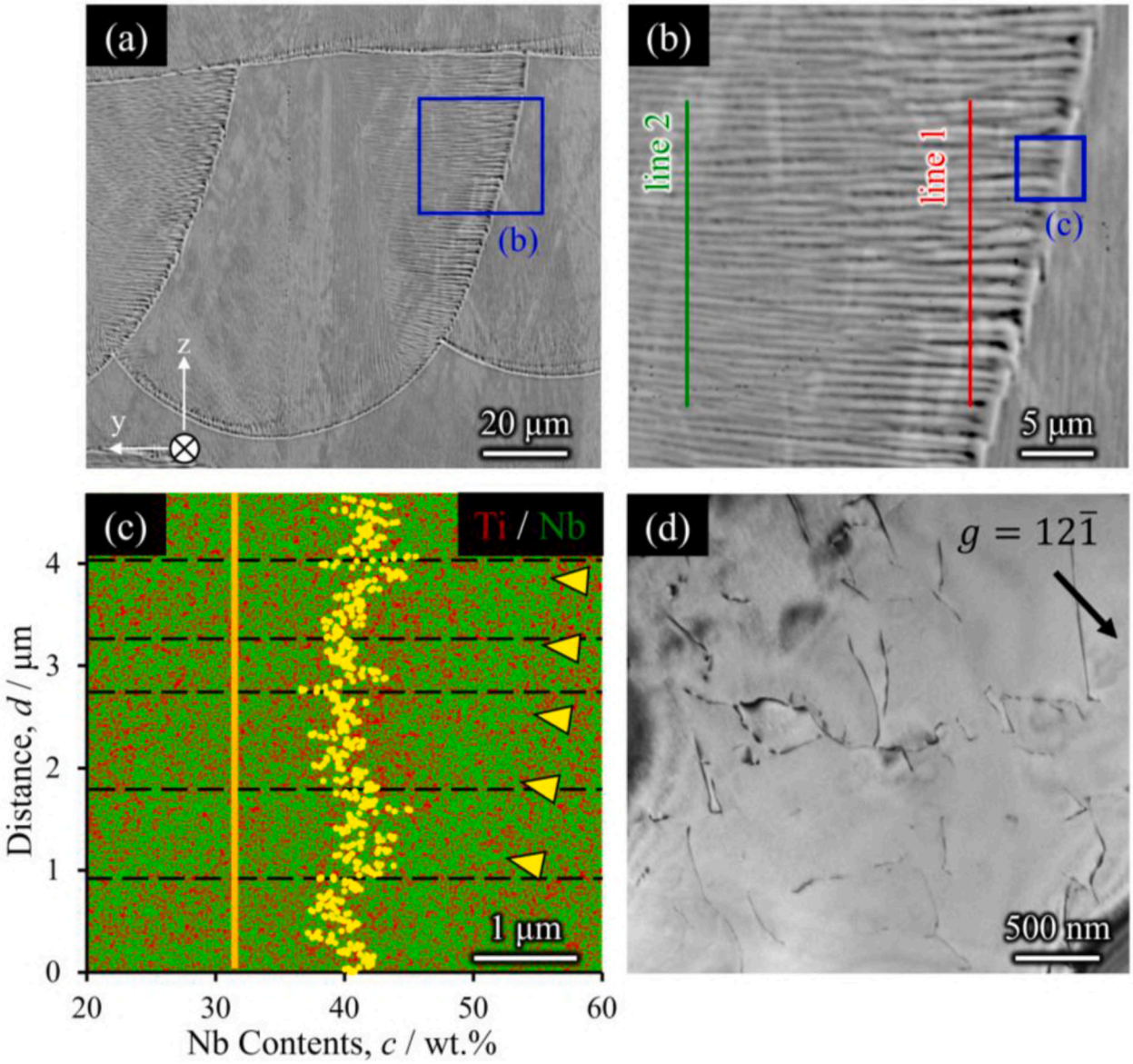

Fig. 7. Microstructural observations for ± XY_SS specimen using SEM and TEM. BSE images observed along the yz-plane with magnifications of (a) ×850 and (b) ×3000. (c) Elemental distribution map analyzed by STEM-EDS at the blue boxed area represented in (b). Nb concentration profile is analyzed along the orange line. Yellow arrowheads trace the edge of the melt pool. (d) Bright-field TEM image for the observation of dislocation conditions. Beam direction is along [101].

and α″ phase precipitates, which influenced the mechanical properties of the alloy. However, the L-PBF-fabricated Ti–42Nb alloy did not form a dislocation cell network. As crystal orientation [20] and metastable phases [53,54] serve as key determinants of elastic and plastic mechanical properties, microstructural control represents a promising approach for regulating the mechanical properties of metastable β-type Ti alloys. In the following section, the contributions of each microstructural feature to the mechanical properties and the mechanisms responsible for microstructure formation are discussed.

4.1. Contributions of microstructures to yield strength

This study successfully controlled the yield strength in the range of 635.3 MPa (±XY_SS) to 791.5 MPa (+120°_SS). The oxygen (0.23 wt.%) and nitrogen (0.032 wt.%) contents were nearly identical among the L-PBF-fabricated specimens because all specimens were fabricated using the same process parameters. Despite these comparable interstitial element concentrations, the specimens with different crystallographic textures exhibited markedly different mechanical properties. These results clearly demonstrate that crystallographic texture plays a significant role in determining the mechanical properties of the present Ti–42Nb alloys.

To evaluate the contributions of microstructures to the yield strength of the alloy, slip-system-driven modeling [55] was applied. The yield strength (σ_y) of a polycrystalline alloy involves several strengthening mechanisms, such as friction stress ($\Delta\sigma_0$), solid solution strengthening (σ_{ss}), GB strengthening (σ_{GB}), and precipitation strengthening ($\Delta\sigma_P$), expressed using Eq. (12).

$$\sigma_y = \Delta\sigma_0 + \Delta\sigma_{SS} + \Delta\sigma_{GB} + \Delta\sigma_P \tag{12}$$

A previous study reported that the combined contribution of friction stress ($\Delta\sigma_0$) and solid-solution strengthening ($\Delta\sigma_{SS}$) was 165 MPa in a Ti–42Nb polycrystal fabricated by arc melting [56]. The value of $\Delta\sigma_0 + \Delta\sigma_{SS}$ was calculated using Eq. (13).

$$\Delta\sigma_0 + \Delta\sigma_{SS} = 165 \times \frac{M_{expt}}{M_{poly}} \tag{13}$$

Herein, the experimental average Taylor factor (M_{expt}) listed in

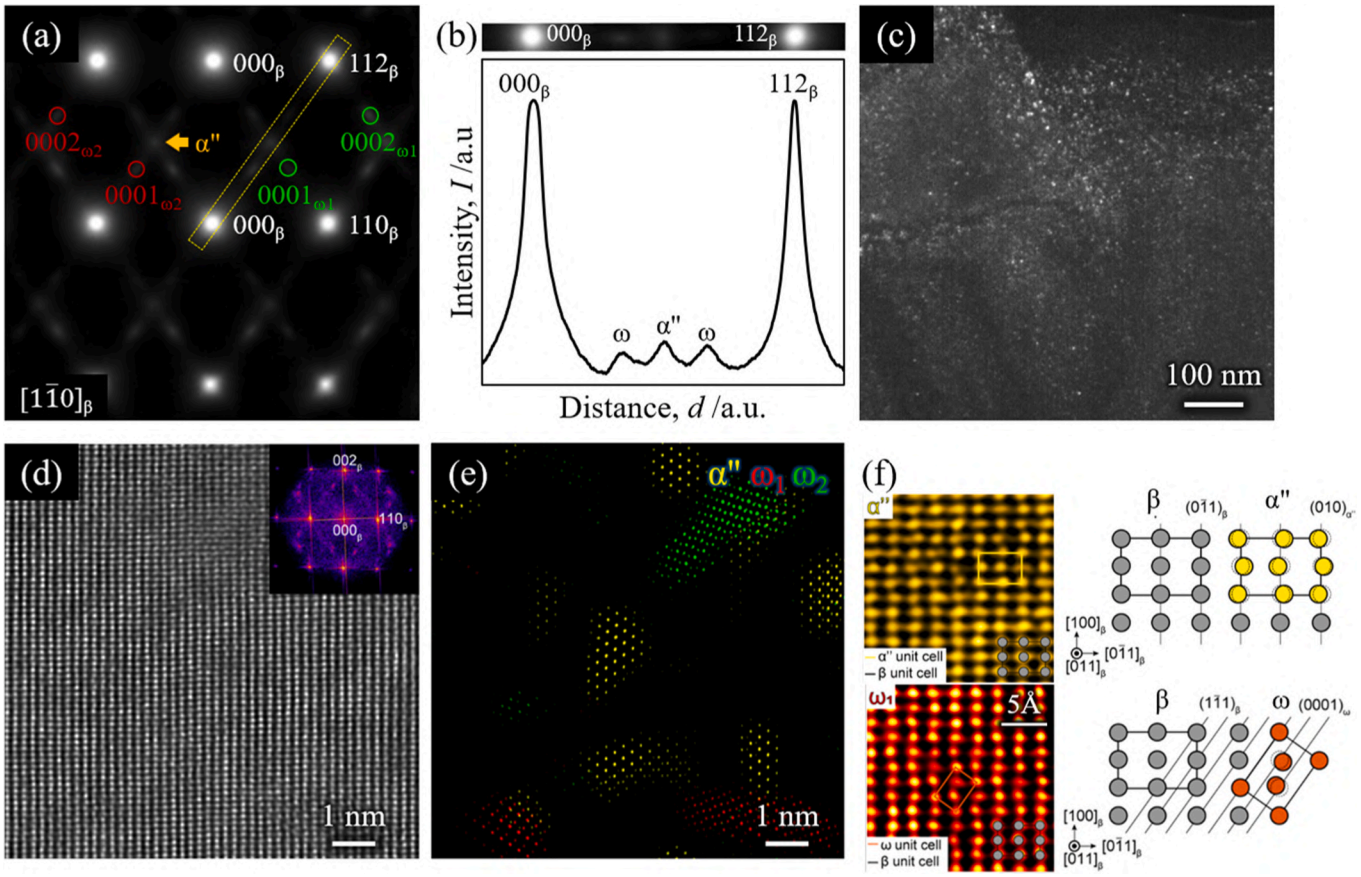

Fig. 8. Characterization of α″ and ω phases in the L-PBF-fabricated Ti–42Nb alloy (±XY_SS specimen). The observations using (a) selected area diffraction pattern along the $[1\bar{1}0]_\beta$, (b) cropped FFT pattern and corresponding intensity profiles, and (c) dark-field TEM image for ω_1 phase. Detailed observations using (d) HAADF-STEM image and corresponding FFT pattern and (e) overlay of IFFT image filtered using reflection spots from α″, two ω phase variants (ω_1 and ω_2) distinguished by their crystal orientation relationships with the β matrix, and the β matrix. (f) Schematic of the orientation relationships among the α″, ω, and β phases.

Table 4
Estimated particle diameter, volume fraction, and interparticle spacing of the ω and α″ phases of the L-PBF-fabricated Ti–42Nb alloy.

Phase	Particle diameter, d_i (nm)	Volume fraction, f_i (%)	Interparticle spacing, l (nm)
ω phase	2.3 ± 0.7	1.2	10.2
α″ phase	1.8 ± 0.4	3.7	4.7

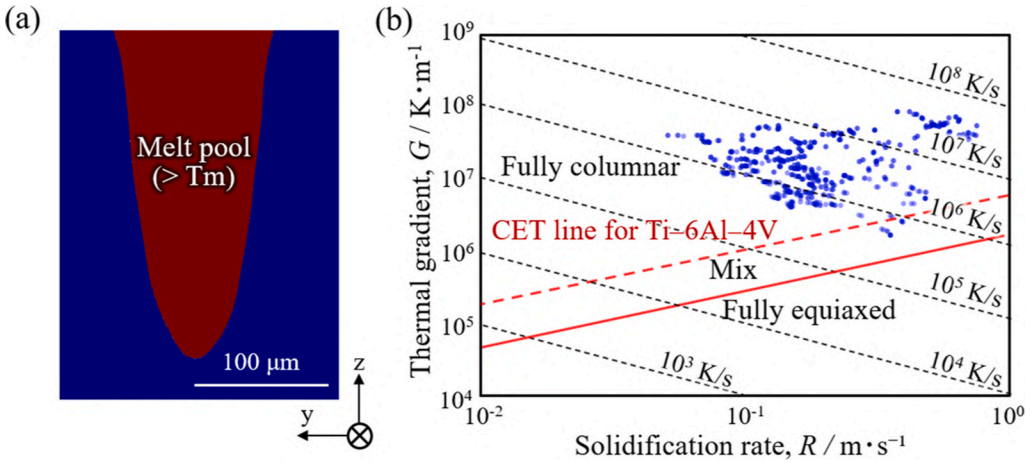

Fig. 9. Solidification condition calculated by thermal diffusion simulation. (a) Calculated melt pool shape formed at laser parameters of $P = 360$ W and $v = 1000$ mm·s^{-1}. (b) Solidification conditions plotted on the G–R map with CET line for Ti-6Al-4V alloy [48].

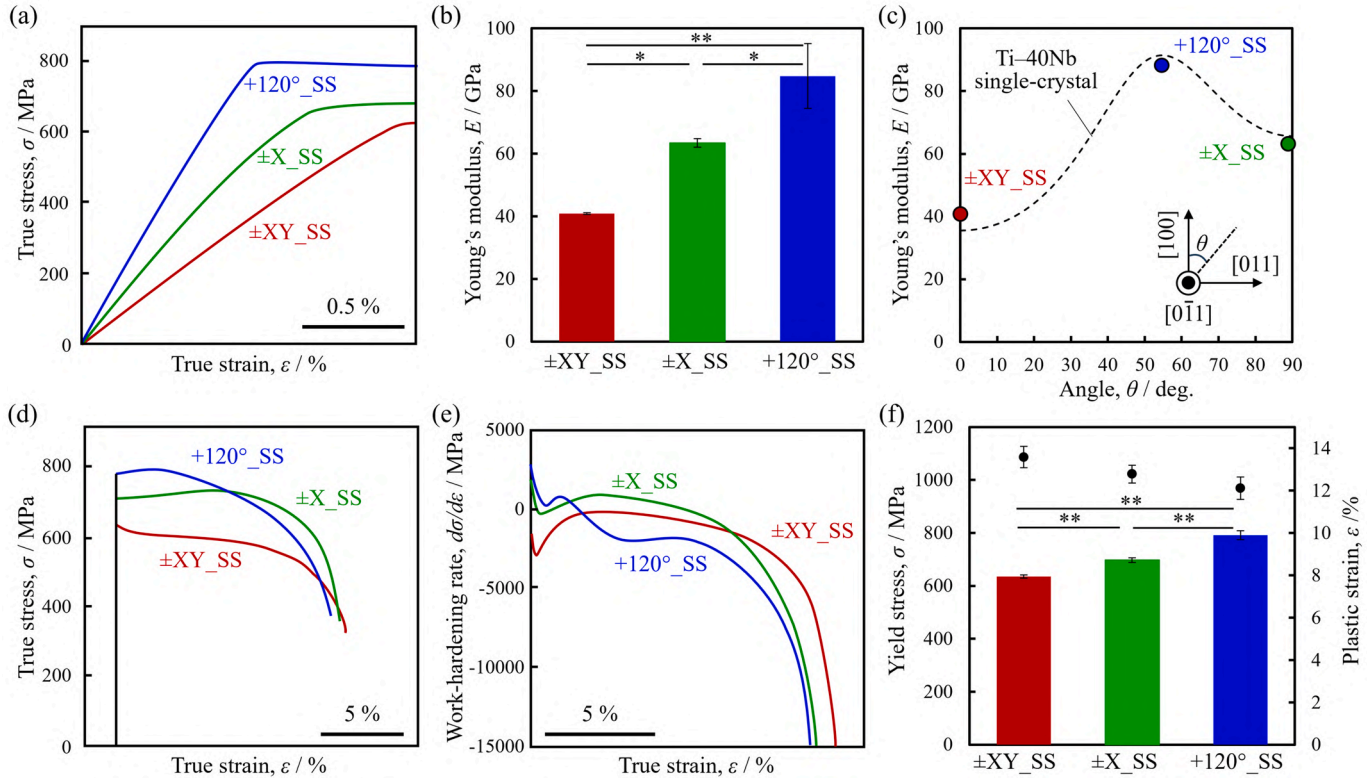

Fig. 10. Mechanical properties measured using the ±XY_SS, ±X_SS, and +120°_SS specimens. (a) Initial portion of the true stress–true strain curve. (b) Young's modulus of the L-PBF-fabricated Ti–42Nb alloy and (c) its comparison with the calculated value in Ti–40Nb single-crystal. (d) True stress-true plastic strain curve and (e) work-hardening rate. (f) Summary of yield stress (bar graphs) and plastic strain (plots). *: $p < 0.05$, **: $p < 0.01$.

Table 5
Experimental average Taylor factor in each specimen.

Scanning strategy	Average Taylor factor, M_{expt} (a.u.)
±XY_SS	2.46
±X_SS	3.11
+120°_SS	3.51

Table 5 and the reported value of M_{poly} (2.75) [57] were used. The calculated values of $\Delta\sigma_0 + \Delta\sigma_{SS}$ are listed in Table 6. The conventional Hall–Petch relationship [58] was used to evaluate $\Delta\sigma_{GB}$, in which the contribution of HAGBs was considered because HAGBs prevent slip propagation across GBs and contribute to strengthening by causing dislocation pile-up.

Furthermore, LAGBs strengthen materials through dislocation interactions [59]. In the specimens obtained in this study, LAGBs accounted for 10–50% of the grain boundaries (Fig. 6), and their contribution cannot be neglected [60]. Therefore, a modified Hall–Petch relationship (Eq. (14)) originally proposed by Luo et al. [61] was used to estimate $\Delta\sigma_{GB}$ for each specimen under different GB conditions, considering the contributions of both HAGBs and LAGBs.

Table 6
Summary of the calculated strengthening increments for each mechanism, the calculated yield strength, and experimental yield strength for the ±XY_SS, ±X_SS, and +120°_SS specimens.

Scanning strategy	$\Delta\sigma_0 + \Delta\sigma_{SS}$ (MPa)	$\Delta\sigma_{GB}$ (MPa)	$\Delta\sigma_{P_\omega}$ (MPa)	$\Delta\sigma_{P_{\alpha''}}$ (MPa)	$\Delta\sigma_{Calc}$ (MPa)	$\Delta\sigma_{Expt}$ (MPa)
±XY_SS	147.6	149.5	218.7	64.9	580.7	635.3
±X_SS	186.6	242.3	276.5	82.1	787.5	697.3
+120°_SS	210.6	222.8	312.1	92.3	837.8	791.5

$$\Delta\sigma_{GB} = M_{expt}\alpha G b\sqrt{\rho_0 + \rho_{LAGB}} + k\cdot\left(\frac{d}{f_{HAGB}}\right)^{\frac{1}{2}}, \quad (14)$$

where M_{expt} is the experimental average Taylor factor (Table 5), α is a constant (0.20), G is the shear modulus of the matrix, and b is the length of the Burgers vector. The values of G and b were obtained from the calculated values for the Ti–39Nb (wt.%) alloy [62]. The dislocation density (ρ_0) was taken as 1.0×10^{13} m^{-2}, previously reported for L-PBF-fabricated Ti–42Nb determined using the electron channeling contrast imaging method [34]. Further, k represented the material constant value (1.24) [63]. Herein, f_{HAGB} denotes the fraction of HAGB (Table 3); and d represents the spacing between the GBs, including LAGB and HAGB, measured using the line intercept method [64]. Assuming that the present specimens were single crystals, the lines were uniquely drawn along the direction of the Burgers vector (<111> for a BCC-structured metal). The details of the method used to determine d are shown in Fig. S3. The measured values of d were 27.9 μm (±XY_SS), 26.8 μm (±X_SS), and 24.1 μm (+120°_SS). The dislocation density (ρ_{LAGB}) stored in LAGBs was estimated using Eq. (15) [61].

$$\rho_{LAGB} = \frac{3(1 - f_{HAGB})\bar{\theta}_{LAGB}}{bd}, \quad (15)$$

where $\bar{\theta}_{LAGB}$ is the average misorientation angle at the LAGB. Based on Eqs. (14) and (15), $\Delta\sigma_{GB}$ was calculated, as listed in Table 6.

To estimate the contributions of the ω and α″ phases to the yield strength, $\Delta\sigma_P$ was calculated for each phase. Precipitation strengthening was expressed by interactions between precipitates and dislocations via the shear or Orowan mechanisms. Of these two mechanisms, the one that yielded the lower $\Delta\sigma_P$ was dominant under the given condition [65]. The theoretical equations for the shear mechanism [44] and the Orowan mechanisms [66] are presented as Eqs. (16) and (17),

respectively.

$$\Delta\sigma_{P\_shear} = 0.9M_{expt}\sqrt{d_i f_i}\,\frac{T}{b}\left(\frac{|G_\beta - G_i|}{G_\beta}\frac{1}{2bln(l/b)}\right)^{\frac{3}{2}}, \quad (16)$$

$$\Delta\sigma_{P\_Orowan} = M_{expt}Gb\left(\sqrt{\frac{32}{3\pi f_i}}\times\frac{d_i}{2} - d_i\right)^{-1}, \quad (17)$$

where G_β and G_i are the shear moduli of the β and precipitated phases, respectively. Previously reported values of G_β and G_i for the Ti–39Nb alloy [62] were used in this study. Herein, T is the linear tension of the dislocation estimated using $G_\beta b^2/2$ and d_i is the precipitate particle size. The measured values of volume fraction for the precipitate phase (f_i) and the distance between the precipitates (l_i) are listed in Table 4. Based on Eqs. (16) and (17), the variations in $\Delta\sigma_P$ as a function of d_i for the ω and α″ phases are summarized in Fig. 11. The results revealed that the critical precipitate size, defined as the intersection of $\Delta\sigma_{P\_shear}$ and $\Delta\sigma_{P\_Orowan}$, differed among specimens for both the ω (Fig. 11(a)–11(c)) and α″ (Fig. 11(d)–11(f)) phases. The measured particle size (Table 4) was applied to evaluate $\Delta\sigma_P$. The obtained results confirmed that the observed precipitate sizes were below the critical size; thus, the shear mechanism was activated in all specimens. The evaluated values of $\Delta\sigma_P$ for the ω and α″ phases, as presented in Table 6, demonstrated that the ω phase posed a greater impact on the yield strength than the α″ phase in the L-PBF-fabricated Ti–42Nb. The estimated strengthening increase associated with the ω phase (200–300 MPa) is within the range reported in previous studies [44,67].

Table 6 summarizes the calculated yield strength, increase associated with each strengthening mechanism, and experimental yield strength. Compared with the experimental data, the calculated yield strength exhibited good agreement within a deviation of ~13%, indicating the relatively high reliability of the calculations for each strengthening mechanism presented in this study. In polycrystalline materials with randomly oriented grains, even if grains with low Taylor factors deform preferentially, deformation is constrained by grain boundaries, after which other grains with low Taylor factors begin to deform. As a result, the average Taylor factor can be used as a representative value that reasonably describes the macroscopic yielding behavior of the material. In contrast, as shown in Fig. S4, the strongly textured specimens obtained in this study exhibited nonuniform Taylor factor distributions characterized by distinct peaks at specific values. Therefore, the use of the average Taylor factor alone may not fully reproduce the macroscopic yielding behavior. For example, the +120°_SS and ±X_SS specimens exhibited average Taylor factors of 3.51 and 3.11, respectively; however, both specimens actually showed bimodal Taylor factor distributions (Fig. S4(b) and S4(c)). In such cases, although grains with lower Taylor factors are more susceptible to local deformation, the strongly textured microstructures, which contain fewer grain boundaries than conventional polycrystalline materials, may provide less constraint against localized deformation. Consequently, the use of the average Taylor factor may lead to an overestimation of the macroscopic yield stress, which could explain why the calculated yield stresses for the +120°_SS and ±X_SS specimens were higher than the experimentally measured values. In contrast, the ±XY_SS specimen exhibited a smaller grain-to-grain variation in Taylor factor (Fig. S4(a)), implying that the average Taylor factor may serve as a more reliable descriptor for this specimen. The discrepancy observed for the ±XY_SS specimen (−8.6%) can be interpreted as representing the inherent limitation of the present yield stress prediction approach.

Notably, ω phase-based precipitation strengthening imposed the greatest impact on yield strength, and the degree of the impact varied depending on crystal orientations. The obtained results demonstrated a considerable effect of ω phase on the strengthening of BCC-structured Ti-

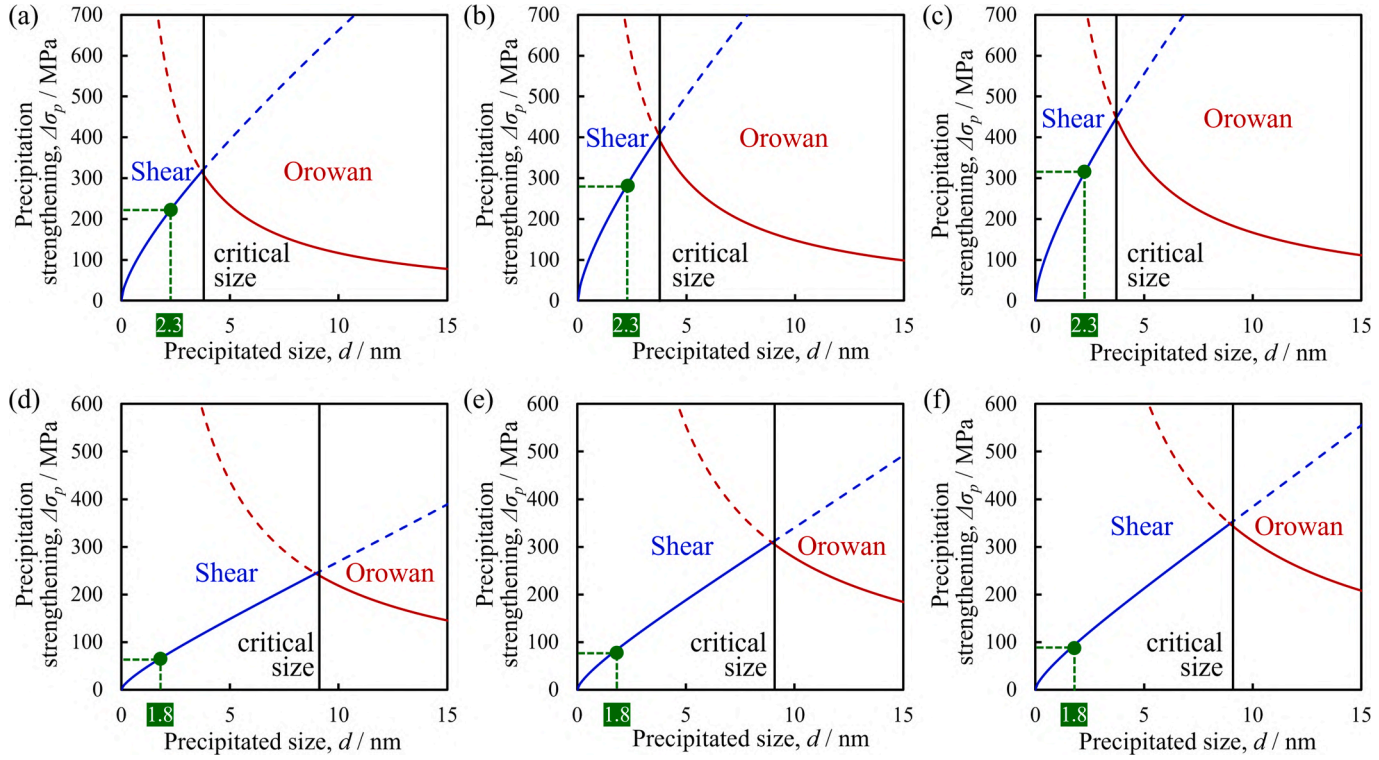

Fig. 11. Variations in precipitation strengthening increments as a function of precipitate size (d_i) for the ω and α″ phases at volume fractions of 1.2% and 3.7%, respectively. The ω phase-based strengthening in (a) ±XY_SS, (b) ±X_SS, and (c) +120°_SS, and α″ phase-based strengthening in (d) ±XY_SS, (e) ±X_SS, and (f) +120°_SS. Red and blue lines represent the increase by shear and Orowan mechanisms, respectively. The black lines represent critical size. $\Delta\sigma_P$ is determined from the intersection (green dot) between the variation curve of strengthening mechanisms and the observed precipitate size, measured as 2.3 and 1.8 nm for the ω and α″ phases, respectively.

alloys.

4.2. Contributions of microstructures to Young's modulus

This study successfully controlled Young's modulus in the range of 40.9 GPa (±XY_SS) to 84.8 GPa (+120°_SS). Notably, in previous studies, the ω phase increases the Young's modulus of β-type Ti alloys [68], whereas the α″ phase does not exhibit such an effect [69]. Nevertheless, the present value of 40.9 GPa in the ±XY_SS specimen was lower than those reported in previous studies listed in Table 7. This study focused on the effect of the ω phase on Young's modulus. To estimate the influence of the precipitated ω phase on Young's modulus, the elastic stiffness of a composite material consisting of the β and ω phases was calculated using the effective mean-field (EMF) theory [78]. The validity of this approach has been demonstrated in two-phase systems, such as the matrix/void system in porous iron [79] and the β/ω system in a Ti–29Nb–13Ta–4.6Zr (wt.%) alloy [68]. In the calculation, a single crystal of the β phase containing the ω phase was approximated as a composite material consisting of a single-crystal β phase matrix and single-crystal ω-phase inclusions. Four ω phase variants with the crystal orientation relationships $\{0001\}_\omega//\{111\}_\beta$ and $<11\bar{2}0>_\omega//<1\bar{1}0>_\beta$ [43] were embedded in the β phase matrix. Furthermore, the elastic properties of a single crystal of the ω phase in pure Ti [80] were used, consistent with a previous study on a Ti–29Nb–13Ta–4.6Zr (wt.%) alloy [68], because the elastic properties of the ω phase in Ti alloys have not been measured due to experimental difficulties. This represents an inherent limitation of the present approach. The shape of the ω phase was approximated as spherical. In the present estimation of the effect of the ω phase on the Ti–42Nb alloy, the elastic properties of the β phase of a Ti–40Nb single crystal [51] were used because the effect of compositional differences between these alloys could be considered negligible. The detailed procedure has been explained in previous studies [78,81]. The relationship between the volume fraction of the ω phase and the calculated Young's modulus of a Ti–40Nb single crystal is shown in Fig. 12(a). The result demonstrated that Young's modulus was strongly dependent on the volume fraction of the ω phase, irrespective of crystal orientation.

However, a volume fraction of only 1.2% of the ω phase resulted in a negligible increase in Young's modulus (Fig. 12(b)). Thus, the low Young's modulus of 40.9 GPa in the ±XY_SS specimen is mainly attributed to the strongly <001>-oriented texture developed via L-PBF.

4.3. Formation mechanism of crystallographic texture

In this study, strong textures with <001>, <011>, and <111> orientations along the z-axis were successfully developed in a Ti–42Nb alloy by employing different scanning strategies. This behavior was consistent with that previously reported for a Ti–15Mo–5Zr–3Al alloy [9]. To discuss the behavior of texture formation, the growth directions of columnar dendrites were observed using SEM (Fig. 13) because the dendrite growth direction corresponded to the <100> orientation in most metals with a cubic crystal system [82]. In the melt pool (highlighted in black lines), <100>-oriented columnar dendrites was aligned along the 0° and 90°-inclined axes in the ±XY_SS specimen (Fig. 13(a), (d), and 13(g)) and along two 45°-inclined axes in the ±X_SS specimen (Fig. 13(b), (e), and 13(h)), with respect to the reference z-axis. The striped contrast observed in the plane parallel to the dendrite growth direction was scarcely observed in the +120°_SS specimen (Fig. 13(c)). Alternatively, <100>-oriented columnar dendrites were assumed to grow within a plane inclined ~35.3° relative to the laser scanning direction, as illustrated in Fig. 13(i) and evidenced by the IPF map (Fig. 13(f)). Furthermore, sub-grain boundaries were observed in all scanning strategies, as represented by the light blue lines in Fig. 13(a)–13(f). These dendrite growth behaviors and the resulting textures were consistent with those observed in Ti–15Mo–5Zr–3Al alloy [9]. Therefore, the development of crystal orientation was attributed to crystal growth that minimized interfacial energy, as proposed in a previous study [9]. To reduce interfacial energy, crystal growth that formed sub-grain boundaries composed of neighboring grains with nearly coherent orientation relationships was considered more favorable than <100>-oriented grain growth governed by heat flow.

Notably, this study, for the first time, demonstrated variations in texture depending on the process parameters and revealed that the behaviors differed among the scanning strategies (Figs. 3–5), despite the fact that the optimal process parameter ($ED = 75\ \mathrm{J{\cdot}mm^{-3}}$) for maximizing the degree of each crystal orientation was common across all scanning strategies. Further, the analysis focused on specimens fabricated with $ED = 62.5\ \mathrm{J{\cdot}mm^{-3}}$ while varying v and P. Notably, the texture weakened in the ±XY_SS and ±X_SS specimens under lower v and higher P conditions, which was the opposite trend observed in the +120°_SS specimen. Such differences in behaviors could be attributed to changes in the melt pool shape and the resultant heat flow direction, particularly as a function of laser scanning speed. A study reported that a higher value of v increases the length of the melt pool tail and the ratio of the tail length (l) to the depth of the melt pool (h) [83]. Thus, the lower v condition, compared with the higher v condition, possibly generated

Table 7
Comparison of mechanical properties between the present Ti–42Nb alloys and previously reported alloys [32–34,38,70–77].

Composition	Process	Yield strength, σ (MPa)	Young's modulus, E (GPa)	Elongation, ε (%)	σ/E (10^{-3})
Ti–15Mo–5Zr–3Al (wt.%) [70]	Cast + ST	838	80	25	10.5
Ti–15Mo(wt.%) [70]	Cast + Annealing	544	78	21	7.0
Ti–35.3Nb–5.1Ta–7.1Zr(wt.%) [70]	Cast	547	55	19	9.9
Ti–29Nb–13Ta–4.6Zr(wt.%) [70]	Cast + Aging	864	80	13.2	10.8
Ti–24Zr–4Nb–8Sn(wt.%) [71]	L-PBF, Unknown	563	53	13.8	10.6
Ti–50Ta(wt.%) [72]	L-PBF, Chessboard_SS	883	75.8	11.7	11.6
Ti–37Nb–6Sn(wt.%) [73]	L-PBF, ±67°_SS	775	66.0	27.5	11.7
Ti–12Mo–6Zr–2Fe(wt.%) [74]	L-PBF, Chessboard_SS	1026	85.7	12.7	12.0
Ti–15Mo–5Zr–3Al(wt.%) [38]	L-PBF, ±XY_SS	752	68.7	26.7	11.0
Ti–35Nb(wt.%) [75]	L-PBF, ±XY_SS	485	72	23.5	7.5
Ti–22Zr–11 Nb–2Sn (at.%) [76]	L-PBF, ±67°_SS	788	51	14.5	15.5
Ti–22Zr–11 Nb–2Sn (at.%) [76]	L-PBF, ±67°_SS + ST	737	46	12.8	16.0
Ti–30Nb/Ti–40Nb gradient [77]	DLD, ± XY_SS	470~	-	10.8	-
Ti–42Nb(wt.%) [32]	L-PBF, Unknown	674	61	11.7	11.0
Ti–42Nb(wt.%) [33]	L-PBF, Unknown	674	44	~17	15.4
Ti–42Nb(wt.%) [34]	L-PBF, ±XY_SS	-	56	-	-
Ti–42Nb(wt.%) (This work)	L-PBF, ±XY_SS	635.3	40.9	13.6	15.5
Ti–42Nb(wt.%) (This work)	L-PBF, ±X_SS	697.3	63.4	12.8	11.0
Ti–42Nb(wt.%) (This work)	L-PBF, +120°_SS	791.5	84.8	12.1	9.3

ST: solution treatment, L-PBF: laser powder bed fusion, DLD: direct laser deposition.

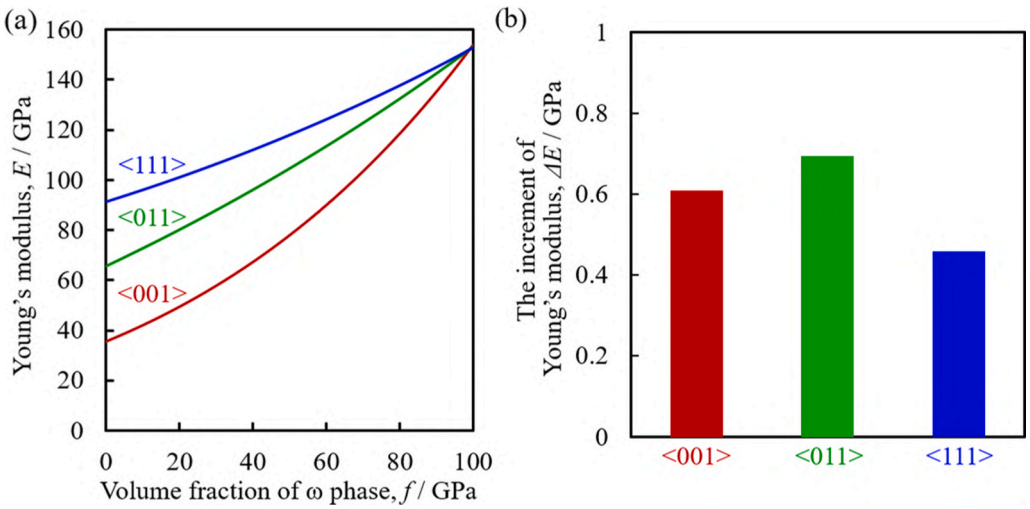

Fig. 12. Effects of the ω phase on Young's modulus in a Ti–40Nb single crystal. (a) Variations in Young's modulus along each crystal orientation as a function of the volume fraction of the ω phase. (b) Increment in Young's modulus induced by the ω phase at a volume fraction of 1.2%, corresponding to the experimental results listed in Table 4.

heat flow along the laser scanning direction despite the same energy density, as illustrated in Fig. 13(j). The growth of columnar dendrites within a plane inclined 35.3° from the z-axis toward the laser scanning direction was necessary for texture development in the +120°_SS specimen (Fig. 13(i)), whereas dendrite growth within a plane perpendicular to the laser scanning direction was favored for texture development in the ±XY_SS (Fig. 13(g)) and ±X_SS (Fig. 13(h)) specimens. Thus, the formation of strong textures was anticipated even under conditions of low v and the resultant low l/h in the +120°_SS specimen, along with those under conditions of high v and the resultant high l/h in the ±XY_SS and ±X_SS specimens. These findings clarified variations in texture as a function of process parameters and provided valuable insights into texture formation behaviors.

4.4. Formation mechanism of fine ω phase in the L-PBF-fabricated Ti–42Nb alloy

As mentioned in Sections 4.1and 4.2, the formation of a small amount of fine ω phase plays a crucial role in realizing reasonable yield strength while maintaining a low Young's modulus in the alloy. Thus, the formation mechanism of the ω phase requires analysis.

Previous studies on Ti–Mo alloy have reported that the size and volume fraction of the ω phase vary depending on the manufacturing process; an increase in cooling rate within the range of 1–10^2 K·s^{-1} leads to refinement of ω-phase precipitates [84]. In this case, the particle size and volume fraction of the ω phase were 15.6 nm and 18.6%, respectively, at 1.8 K·s^{-1} (air cooling). These values decreased to 5.9 nm and 7.0%, respectively, at 45 K·s^{-1} (water quenching), indicating a distinct relationship between the cooling rate and the precipitation behavior of the ω phase. Another study on Ti–18Mo (wt.%) alloys reported that the particle size of the ω phase in a solution heat-treated alloy increased from ~10 nm to 80 nm after annealing at 475 °C for 48 h [85]. Furthermore, a study using differential scanning calorimetry (DSC) reported that the ω phase could potentially transform into the β phase when the temperature rose above the reverse transformation temperature (~485 °C) in a Ti–33Nb (wt.%) alloy [86]. Conversely, in the first step of the L-PBF process, the powder bed region was subjected to high temperatures, melted after laser irradiation, and subsequently solidified through rapid cooling, as estimated in Section 3.5. In the subsequent step, laser irradiation of adjacent and upper regions exposed the already solidified material to high temperatures, causing partial melting and resolidification, while the rest of the regions experienced thermal effects. However, high temperatures were maintained for only a substantially short duration, as supported by a simulation study [87]. Thus, the L-PBF process exposed the material to a unique thermal history. Although the detailed formation mechanism of the ω phase during the L-PBF process remains unclear, this study, consistent with previous reports [29,47], supports the conclusion that L-PBF is an effective means of forming fine ω-phase precipitates. The effects of the unique thermal history, including rapid cooling during solidification and subsequent thermal exposure, on the precipitation behavior of the ω phase require research solutions in future work.

4.5. Potential for application as a biomaterial

Metallic biomaterials used as load-bearing medical implants must exhibit mechanical osteocompatibility and biocompatibility, along with a well-balanced combination of strength, ductility, and fatigue resistance [70]. Stress shielding, causing dysfunction of bone due to bone loss and deterioration of bone quality [88], often occurs because the Young's modulus of metallic implants is excessively higher than that of natural bone. To address this issue, two primary strategies can be considered: (i) reducing the intrinsic Young's modulus of the material, or (ii) decreasing the implant thickness to lower the effective structural stiffness. In the latter approach, a high σ_y/E indicates greater flexibility to reduce the modulus while maintaining sufficient strength through material thinning. Accordingly, σ_y/E serves as a quantitative indicator of mechanical osteocompatibility [89].

The Ti–42Nb alloy fabricated using ± XY_SS exhibited a low Young's modulus of 40.9 GPa, which is comparable to that of bone tissue (~30 GPa) [90], along with an acceptable yield strength (635.3 MPa) and plastic strain (13.6%) for biomedical applications. This resulted in a high σ_y/E value of 15.5×10^{-3}, which is one of the highest values listed in Table 7. Moreover, this alloy demonstrated excellent biocompatibility in an *in vitro* cell culture experiment, as described in Appendix 1. The cell density after 24 h of culture on the alloy was comparable to that on CP–Ti and higher than that on SUS316L (Fig. S5). Therefore, the texture-controlled Ti–42Nb alloy can serve as a promising biomaterial, in which a <001>-oriented texture significantly reduces Young's modulus, while a small amount of fine ω phase increases yield strength without adversely affecting Young's modulus.

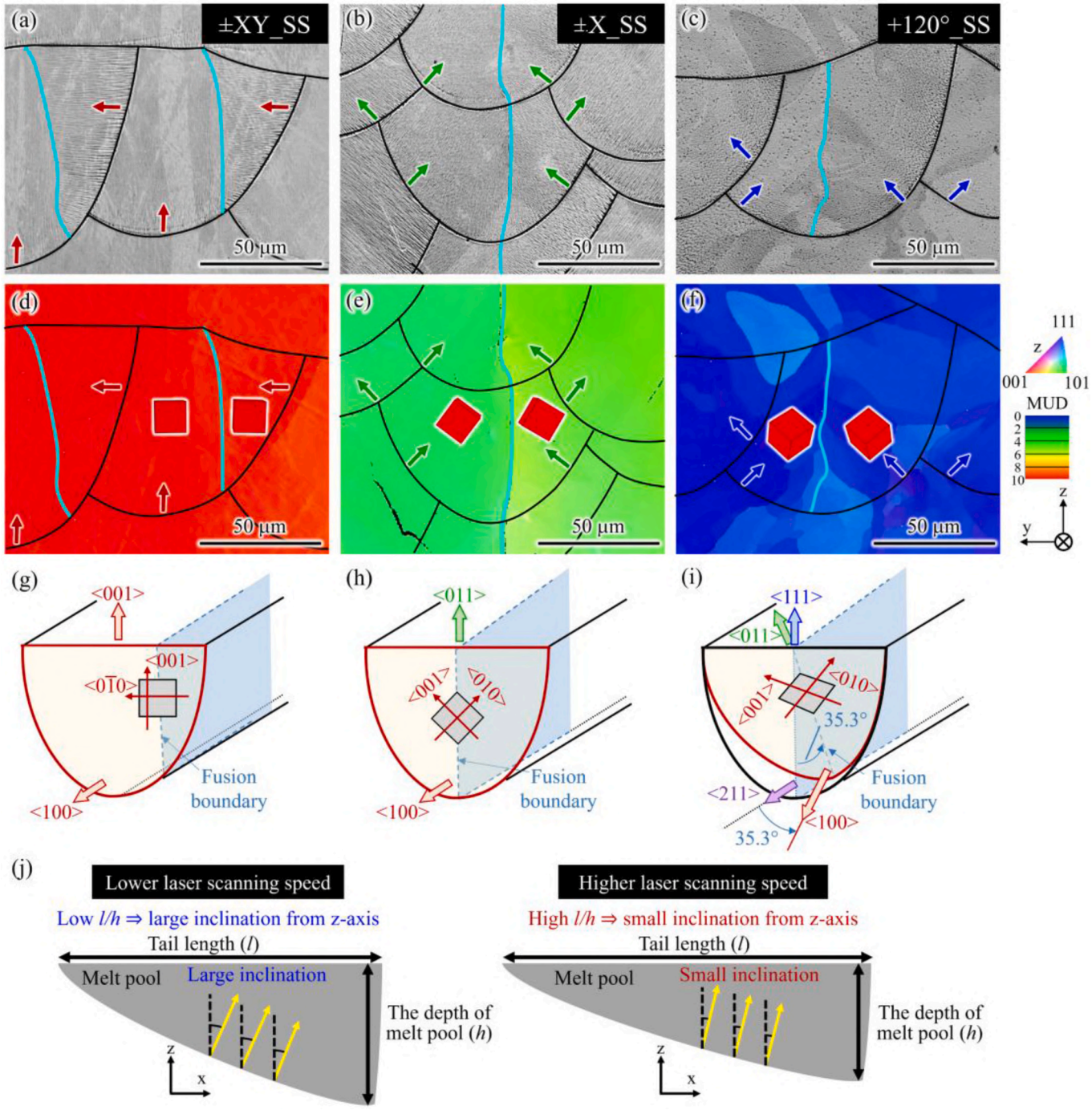

Fig. 13. Crystal growth directions and their relations to texture formation. BSE images and the corresponding IPF maps taken along the yz-plane of (a, d) ±XY_SS, (b, e) ±X_SS, and (c, f) +120°_SS. The IPF maps represent the projection along the z-axis. Arrows indicate the <100>-oriented dendrite growth directions in (a), (b), (d), and (e). Arrows in (c) and (f) indicate the dendrite growth direction on the plane inclined at 35.3° from the z-axis. The schematic cubes represent three-dimensional crystal orientation in (d–f). Melt pool edges and sub-grain boundaries are highlighted in black and light blue lines, respectively, in (a–f). (g–i) Schematics of the crystal growth directions and the formation of fusion boundaries. (j) Schematic of the melt pool formed under conditions of higher and lower laser scanning speed.

5. Conclusions

Using L-PBF, this study fabricated Ti–42Nb alloys with controlled crystallographic textures, columnar dendrites without a distinct dislocation network, and nanosized ω and α″ precipitates, and systematically evaluated the effects of these microstructural features on mechanical properties. The conclusions of this study are summarized as follows:

i) Three types of strong textures with <001>, <011>, and <111> orientations along the building direction were successfully obtained by employing different scanning strategies. These textures significantly influenced both Young's modulus and yield strength through crystal-orientation-dependent elastic and plastic properties. Hence, the <001>-oriented specimen exhibited a low Young's modulus ($E = 40.9$ GPa), reasonable yield strength ($\sigma = 635.3$ MPa), and consequently achieved a high yield strength-to-Young's modulus ratio (15.5×10^{-3}).

ii) SEM and TEM observations clarified the formation of columnar dendrite with slight elemental segregation, the absence of organized dislocation cells, and fine ω and α″ phase precipitates present in small amounts. In the <001>-oriented specimen, the ω phase exhibited an average particle size of 2.3 nm and a volume fraction of 1.2%. Calculations revealed that the ω phase contributed significantly to yield strength enhancement ($\Delta\sigma_{P_\omega} = 218.7$ MPa), while having a negligible effect on Young's modulus ($\Delta E = 0.6$ GPa).

iii) Based on the combined effects of texture control and fine ω phase formation in the Ti–42Nb alloy, the <001>-oriented specimen demonstrated excellent mechanical osteocompatibility and good biocompatibility. Therefore, the microstructure-controlled Ti–42Nb alloy represents a promising biomaterial for orthopedic implant applications.

Data statement

Data will be available upon request.

Role of the funding source

The funders played no role in the study design, data collection, data analysis, data interpretation, or writing of the reports.

CRediT authorship contribution statement

Keitaro Miyasawa: Conceptualization, Formal analysis, Investigation, Methodology, Software, Writing – original draft. **Ryosuke Ozasa:** Conceptualization, Data curation, Formal analysis, Funding acquisition, Investigation, Methodology, Software, Supervision, Visualization, Writing – review & editing. **Daisuke Egusa:** Investigation, Methodology. **Eiji Abe:** Investigation, Validation. **Masakazu Tane:** Formal analysis, Methodology, Software. **Kazuhisa Sato:** Investigation, Methodology. **Pan Wang:** Validation, Writing – review & editing. **Takayoshi Nakano:** Conceptualization, Funding acquisition, Project administration, Resources, Supervision, Validation, Writing – review & editing.

Declaration of competing interest

The authors declare the following personal relationships which may be considered as potential competing interests: Pan Wang is one of associate editors of Smart Materials in Manufacturing. If there are other authors, they declare that they have no known competing financial interests or personal relationships that could have appeared to influence the work reported in this paper.

Acknowledgments

This work was partially supported by CREST-Nanomechanics: Elucidation of Macroscale Mechanical Properties Based on Understanding Nanoscale Dynamics for Innovative Mechanical Materials (Grant No. JPMJCR2194) from the Japan Science and Technology Agency and Grants-in-Aid for Scientific Research (Grant Nos. 23K23080, 25K00051, and 23H00235) from the Japan Society for the Promotion of Science (JSPS). A part of this work was supported by ARIM Project of the Ministry of Education, Culture, Sports, Science and Technology, Japan (MEXT) , Grant No. JPMXP1223OS0043 at the Research Center for UHVEM (Nanotechnology Open Facilities) in The University of Osaka. The authors thank Mr. K. Kimura for his help with the operation of L-PBF machine and Dr. S. Takagi for his help with FIB microsampling.

Appendix A. Supplementary data

Supplementary data to this article can be found online at https://doi.org/10.1016/j.smmf.2026.100148.

References

[1] J. Plocher, A. Panesar, Review on design and structural optimisation in additive manufacturing: towards next-generation lightweight structures, Mater. Des. 183 (2019) 108164, https://doi.org/10.1016/j.matdes.2019.108164.
[2] N. Ikeo, H. Fukuda, A. Matsugaki, T. Inoue, A. Serizawa, T. Matsuzaka, T. Ishimoto, R. Ozasa, O. Gokcekaya, T. Nakano, 3D puzzle in cube pattern for anisotropic/isotropic mechanical control of structure fabricated by metal additive manufacturing, Crystals 11 (2021) 959, https://doi.org/10.3390/cryst11080959.
[3] N. Ikeo, T. Matsumi, T. Ishimoto, R. Ozasa, A. Matsugaki, T. Matsuzaka, O. Gokcekaya, Y. Takigawa, T. Nakano, Fabrication of Ti-Alloy powder/solid composite with uniaxial anisotropy by introducing unidirectional honeycomb structure via electron beam powder bed fusion, Crystals 11 (2021) 1074, https://doi.org/10.3390/cryst11091074.
[4] C. Wang, C.-N. Sun, T. Chang, X. Liang, N. Ma, P. Wang, Orientation-dependent residual stress governs anisotropic warpage in laser powder bed fusion stainless steel: experimental analysis and predictive modelling, Addit. Manuf. 121 (2026) 105158, https://doi.org/10.1016/j.addma.2026.105158.
[5] Z.-Y. Wu, Y.-J. Liu, H.-W. Bai, X. Wu, Y.-H. Gao, X.-C. Liu, J.-C. Wang, Q. Wang, Microstructure and mechanical behavior of rhombic dodecahedron-structured porous β-Ti composites fabricated via laser powder bed fusion, J. Mater. Res. Technol. 31 (2024) 298–310, https://doi.org/10.1016/j.jmrt.2024.06.077.
[6] M.K. Yadav, K. Praveenkumar, R.H. Shukla, S. Nilawar, C.S. Perugu, K. Chatterjee, S. Suwas, J. Jayaraj, K.G. Prashanth, Novel partially biodegradable Ti-6Al-4V/Zn composites fabricated through hybrid additive manufacturing and powder metallurgy, Adv. Light Mater. 1 (2026) 1–18, https://doi.org/10.1016/j.almate.2026.03.001.
[7] Q. Liu, Y. Zhang, W. Chen, P. He, Y. Tian, Y. Liu, Y. Dou, H. Bian, J. Yang, Q. Yang, X. Li, Bioactive and fatigue-resistant Ti–Ta alloy by additive manufacturing for orthopedic applications, Smart Mater. Manuf. 3 (2025) 100086, https://doi.org/10.1016/j.smmf.2025.100086.
[8] K. Hagihara, T. Nakano, Control of anisotropic crystallographic texture in powder bed fusion additive manufacturing of metals and ceramics—A review, JOM 74 (2022) 1760–1773, https://doi.org/10.1007/s11837-021-04966-7.
[9] T. Ishimoto, N. Morita, R. Ozasa, A. Matsugaki, O. Gokcekaya, S. Higashino, M. Tane, T. Mayama, K. Cho, H.Y. Yasuda, M. Okugawa, Y. Koizumi, M. Yoshiya, D. Egusa, T. Sasaki, E. Abe, H. Kimizuka, N. Ikeo, T. Nakano, Superimpositional design of crystallographic textures and macroscopic shapes via metal additive manufacturing—Game-change in component design, Acta Mater. 286 (2025) 120709, https://doi.org/10.1016/j.actamat.2025.120709.
[10] O. Gokcekaya, T. Ishimoto, S. Hibino, J. Yasutomi, T. Narushima, T. Nakano, Unique crystallographic texture formation in inconel 718 by laser powder bed fusion and its effect on mechanical anisotropy, Acta Mater. 212 (2021) 116876, https://doi.org/10.1016/j.actamat.2021.116876.
[11] R. Ozasa, Y. Kizawa, K. Okawa, K. Hagihara, K. Sato, T. Matsumoto, T. Tokunaga, N. Ikeo, V. Srimaneepong, P. Wang, D.J. Jensen, T. Nakano, Design of a novel scanning strategy for formation of extremely strong textures in hexagonal materials through laser powder bed fusion, Mater. Des. (2026) 116307, https://doi.org/10.1016/j.matdes.2026.116307.
[12] Y.S. Kim, R. Ozasa, K. Sato, O. Gokcekaya, T. Nakano, Design and development of a novel non-equiatomic Ti-Nb-Mo-Ta-W refractory high entropy alloy with a single-phase body-centered cubic structure, Scr. Mater. 252 (2024) 116260, https://doi.org/10.1016/j.scriptamat.2024.116260.
[13] M. Cagirici, S. Guo, J. Ding, U. Ramamurty, P. Wang, Additive manufacturing of high-entropy alloys: current status and challenges, Smart Mater. Manuf. 2 (2024) 100058, https://doi.org/10.1016/j.smmf.2024.100058.
[14] T. Voisin, J.-B. Forien, A. Perron, S. Aubry, N. Bertin, A. Samanta, A. Baker, Y. M. Wang, New insights on cellular structures strengthening mechanisms and thermal stability of an austenitic stainless steel fabricated by laser powder-bed-fusion, Acta Mater. 203 (2021) 116476, https://doi.org/10.1016/j.actamat.2020.11.018.
[15] Y.M. Wang, T. Voisin, J.T. McKeown, J. Ye, N.P. Calta, Z. Li, Z. Zeng, Y. Zhang, W. Chen, T.T. Roehling, R.T. Ott, M.K. Santala, P.J. Depond, M.J. Matthews, A. V. Hamza, T. Zhu, Additively manufactured hierarchical stainless steels with high strength and ductility, Nat. Mater. 17 (2018) 63–71, https://doi.org/10.1038/nmat5021.
[16] D. Riabov, A. Leicht, J. Ahlström, E. Hryha, Investigation of the strengthening mechanism in 316L stainless steel produced with laser powder bed fusion, Mater. Sci. Eng., A 822 (2021) 141699, https://doi.org/10.1016/j.msea.2021.141699.
[17] X. Lyu, J. Zhang, F. Weber, A. Bezold, C. Broeckmann, Mechanical behaviours of the hierarchical microstructure of PBF-LB/M 316L SS during high cycle fatigue, Mater. Sci. Eng., A 922 (2025) 147652, https://doi.org/10.1016/j.msea.2024.147652.
[18] G. Luo, H. Chen, Y. Li, C. Yang, L. Hu, S. Ma, H. Wang, Z. Chen, Y. Wu, M. Wang, H. Wang, Improved elevated-temperature strength and thermal stability of additive manufactured r alloys reinforced by cellular structures, Addit. Manuf. 90 (2024) 104313, https://doi.org/10.1016/j.addma.2024.104313.
[19] R. Li, D. Kong, K. He, Y. Zhou, C. Dong, Improved passivation ability via tuning dislocation cell substructures for FeCoCrNiMn high-entropy alloy fabricated by laser powder bed fusion, Appl. Surf. Sci. 621 (2023) 156856, https://doi.org/10.1016/j.apsusc.2023.156856.
[20] Y.W. Zhang, S.J. Li, E.G. Obbard, H. Wang, S.C. Wang, Y.L. Hao, R. Yang, Elastic properties of Ti–24Nb–4Zr–8Sn single crystals with bcc crystal structure, Acta Mater. 59 (2011) 3081–3090, https://doi.org/10.1016/j.actamat.2011.01.048.
[21] S.-H. Lee, M. Todai, M. Tane, K. Hagihara, H. Nakajima, T. Nakano, Biocompatible low Young's modulus achieved by strong crystallographic elastic anisotropy in

Ti–15Mo–5Zr–3Al alloy single crystal, J. Mech. Behav. Biomed. Mater. 14 (2012) 48–54, https://doi.org/10.1016/j.jmbbm.2012.05.005.
[22] M. Tane, K. Morita, E. Miyoshi, T. Hiramatsu, Low Young's modulus achieved by anelastic relaxation arising from reversible atomic shuffling in bcc Ti–Nb alloys, Acta Mater. 307 (2026) 121969, https://doi.org/10.1016/j.actamat.2026.121969.
[23] S. Pilz, A. Hariharan, F. Günther, M. Zimmermann, A. Gebert, Influence of isothermal omega precipitation aging on deformation mechanisms and mechanical properties of a β-type Ti-Nb alloy, J. Alloys Compd. 930 (2023) 167309, https://doi.org/10.1016/j.jallcom.2022.167309.
[24] H.Y. Kim, Y. Ikehara, J.I. Kim, H. Hosoda, S. Miyazaki, Martensitic transformation, shape memory effect and superelasticity of Ti–Nb binary alloys, Acta Mater. 54 (2006) 2419–2429, https://doi.org/10.1016/j.actamat.2006.01.019.
[25] P. Castany, Y. Yang, E. Bertrand, T. Gloriant, Reversion of a Parent {130}⟨310⟩α" Martensitic Twinning System at the Origin of {332}⟨113⟩$_\beta$ Twins Observed in Metastable β Titanium Alloys, Phys. Rev. Lett. 117 (2016) 245501, https://doi.org/10.1103/PhysRevLett.117.245501.
[26] M. Tahara, H.Y. Kim, H. Hosoda, S. Miyazaki, Cyclic deformation behavior of a Ti–26 at.% Nb alloy, Acta Mater. 57 (2009) 2461–2469, https://doi.org/10.1016/j.actamat.2009.01.037.
[27] Y. Al-Zain, H.Y. Kim, T. Koyano, H. Hosoda, S. Miyazaki, A comparative study on the effects of the ω and α phases on the temperature dependence of shape memory behavior of a Ti–27Nb alloy, Scr. Mater. 103 (2015) 37–40, https://doi.org/10.1016/j.scriptamat.2015.02.032.
[28] J.I. Kim, H.Y. Kim, H. Hosoda, S. Miyazaki, Shape memory behavior of Ti–22Nb–(0.5–2.0)O(at%) biomedical alloys, Mater. Trans. 46 (2005) 852–857, https://doi.org/10.2320/matertrans.46.852.
[29] S.A. Mantri, M.S.K.K.Y. Nartu, S. Dasari, A. Sharma, P. Agrawal, R. Salloom, F. Sun, E. Ivanov, K. Cho, B. McWilliams, S.G. Srinivasan, N.B. Dahotre, F. Prima, R. Banerjee, Suppression and reactivation of transformation and twinning induced plasticity in laser powder bed fusion additively manufactured Ti-10V-2Fe-3Al, Addit. Manuf. 48 (2021) 102406, https://doi.org/10.1016/j.addma.2021.102406.
[30] H. Schaal, P. Castany, T. Gloriant, Characterization of the stress-induced martensitic transformation in a ti-zr-nb-sn biomedical alloy manufactured by laser powder bed fusion, Materialia 45 (2026) 102670, https://doi.org/10.1016/j.mtla.2026.102670.
[31] S. Huang, P. Kumar, W.Y. Yeong, R.L. Narayan, U. Ramamurty, Fracture behavior of laser powder bed fusion fabricated Ti41Nb via *in-situ* alloying, Acta Mater. 225 (2022) 117593, https://doi.org/10.1016/j.actamat.2021.117593.
[32] C. Schulze, M. Weinmann, C. Schweigel, O. Keßler, R. Bader, Mechanical properties of a newly additive manufactured implant material based on Ti-42Nb, Materials 11 (2018) 124, https://doi.org/10.3390/ma11010124.
[33] S. Pilz, T. Gustmann, F. Günther, M. Zimmermann, U. Kühn, A. Gebert, Controlling the Young's modulus of a ß-type Ti-Nb alloy via strong texturing by LPBF, Mater. Des. 216 (2022) 110516, https://doi.org/10.1016/j.matdes.2022.110516.
[34] S. Tekumalla, M. Seita, S. Zaefferer, Delineating dislocation structures and residual stresses in additively manufactured alloys, Acta Mater. 262 (2024) 119413, https://doi.org/10.1016/j.actamat.2023.119413.
[35] T. Ishimoto, K. Hagihara, K. Hisamoto, T. Nakano, Stability of crystallographic texture in laser powder bed fusion: understanding the competition of crystal growth using a single crystalline seed, Addit. Manuf. 43 (2021) 102004, https://doi.org/10.1016/j.addma.2021.102004.
[36] M. Todai, T. Nakano, T. Liu, H.Y. Yasuda, K. Hagihara, K. Cho, M. Ueda, M. Takeyama, Effect of building direction on the microstructure and tensile properties of Ti-48Al-2Cr-2Nb alloy additively manufactured by electron beam melting, Addit. Manuf. 13 (2017) 61–70, https://doi.org/10.1016/j.addma.2016.11.001.
[37] T. Todo, T. Ishimoto, O. Gokcekaya, J. Oh, T. Nakano, Single crystalline-like crystallographic texture formation of pure tungsten through laser powder bed fusion, Scr. Mater. 206 (2022) 114252, https://doi.org/10.1016/j.scriptamat.2021.114252.
[38] S.-H. Sun, K. Hagihara, T. Ishimoto, R. Suganuma, Y.-F. Xue, T. Nakano, Comparison of microstructure, crystallographic texture, and mechanical properties in Ti–15Mo–5Zr–3Al alloys fabricated via electron and laser beam powder bed fusion technologies, Addit. Manuf. 47 (2021) 102329, https://doi.org/10.1016/j.addma.2021.102329.
[39] A. Takase, T. Ishimoto, N. Morita, N. Ikeo, T. Nakano, Comparison of phase characteristics and residual stresses in Ti-6Al-4V alloy manufactured by laser powder bed fusion (L-PBF) and electron beam powder bed fusion (EB-PBF) techniques, Crystals 11 (2021) 796, https://doi.org/10.3390/cryst11070796.
[40] H.J. Willy, X. Li, Z. Chen, T.S. Herng, S. Chang, C.Y.A. Ong, C. Li, J. Ding, Model of laser energy absorption adjusted to optical measurements with effective use in finite element simulation of selective laser melting, Mater. Des. 157 (2018) 24–34, https://doi.org/10.1016/j.matdes.2018.07.029.
[41] G.L. Knapp, N. Raghavan, A. Plotkowski, T. DebRoy, Experiments and simulations on solidification microstructure for inconel 718 in powder bed fusion electron beam additive manufacturing, Addit. Manuf. 25 (2019) 511–521, https://doi.org/10.1016/j.addma.2018.12.001.
[42] B.A. Hatt, V.G. Rivlin, Phase transformations in superconducting Ti-Nb alloys, J. Phys. Appl. Phys. 1 (1968) 1145, https://doi.org/10.1088/0022-3727/1/9/307.
[43] S.K. Sikka, Y.K. Vohra, R. Chidambaram, Omega phase in materials, Prog. Mater. Sci. 27 (1982) 245–310, https://doi.org/10.1016/0079-6425(82)90002-0.
[44] M.J. Lai, T. Li, D. Raabe, ω phase acts as a switch between dislocation channeling and joint twinning- and transformation-induced plasticity in a metastable β titanium alloy, Acta Mater. 151 (2018) 67–77, https://doi.org/10.1016/j.actamat.2018.03.053.
[45] W. Chen, K. Li, G. Yu, J. Ren, Y. Zha, J. Sun, Deformation twinning-induced single-variant ω-plates in metastable β-Ti alloys containing athermal ω-precipitates, J. Mater. Sci. 56 (2021) 7710–7726, https://doi.org/10.1007/s10853-020-05706-z.
[46] Y.W. Chai, H.Y. Kim, H. Hosoda, S. Miyazaki, Self-accommodation in Ti–Nb shape memory alloys, Acta Mater. 57 (2009) 4054–4064, https://doi.org/10.1016/j.actamat.2009.04.051.
[47] Y. Liu, L. Xu, C. Qiu, Development of an additively manufactured metastable beta titanium alloy with a fully equiaxed grain structure and ultrahigh yield strength, Addit. Manuf. 60 (2022) 103208, https://doi.org/10.1016/j.addma.2022.103208.
[48] P.A. Kobryn, S.L. Semiatin, Microstructure and texture evolution during solidification processing of Ti–6Al–4V, J. Mater. Process. Technol. 135 (2003) 330–339, https://doi.org/10.1016/S0924-0136(02)00865-8.
[49] W. Kurz, R. Trivedi, Banded solidification microstructures, Metall. Mater. Trans. A 27 (1996) 625–634, https://doi.org/10.1007/BF02648951.
[50] T. Nagase, M. Matsumoto, Y. Fujii, Microstructure of Ti-Ag immiscible alloys with liquid phase separation, J. Alloys Compd. 738 (2018) 440–447, https://doi.org/10.1016/j.jallcom.2017.12.138.
[51] H.W. Jeong, Y.S. Yoo, Y.T. Lee, J.K. Park, Elastic softening behavior of Ti–Nb single crystal near martensitic transformation temperature, J. Appl. Phys. 108 (2010) 063515, https://doi.org/10.1063/1.3486212.
[52] D. Banerjee, J.C. Williams, Perspectives on titanium science and technology, Acta Mater. 61 (2013) 844–879, https://doi.org/10.1016/j.actamat.2012.10.043.
[53] N. Ramachandiran, H. Asgari, F. Dibia, R. Eybel, W. Muhammad, A. Gerlich, E. Toyserkani, Effects of post heat treatment on microstructure and mechanical properties of Ti5553 parts made by laser powder bed fusion, J. Alloys Compd. 938 (2023) 168616, https://doi.org/10.1016/j.jallcom.2022.168616.
[54] D.-F. Li, C.-G. Bai, Z.-Q. Zhang, R. Wang, N. Li, R. Yang, α'' martensite engineering: a strategy to achieve high yield strength and low yield ratio synergy for dual-phase titanium alloy, Mater. Des. 239 (2024) 112764, https://doi.org/10.1016/j.matdes.2024.112764.
[55] N. Kamikawa, K. Sato, G. Miyamoto, M. Murayama, N. Sekido, K. Tsuzaki, T. Furuhara, Stress–strain behavior of ferrite and bainite with nano-precipitation in low carbon steels, Acta Mater. 83 (2015) 383–396, https://doi.org/10.1016/j.actamat.2014.10.010.
[56] H. Hosoda, Y. Horiuchi, T. Inamura, K. Wakashima, H.Y. Kim, S. Miyazaki, Effect of carbon addition of shape memory properties of TiNb alloys, Mater. Sci. Forum 638–642 (2010) 2046–2051. https://doi.org/10.4028/www.scientific.net/MSF.638-642.2046.
[57] G.Y. Chin, W.L. Mammel, Computer solutions of taylor analysis for axisymmetric flow, Trans Met Sci AIME 239 (1967) 1400–1405.
[58] E.O. Hall, The deformation and ageing of mild steel: III discussion of results, Proc. Phys. Soc. B 64 (1951) 747, https://doi.org/10.1088/0370-1301/64/9/303.
[59] W.T. Read, W. Shockley, Dislocation models of crystal grain boundaries, Phys. Rev. 78 (1950) 275–289, https://doi.org/10.1103/PhysRev.78.275.
[60] S. Chen, Q. Yu, The role of low angle grain boundary in deformation of titanium and its size effect, Scr. Mater. 163 (2019) 148–151, https://doi.org/10.1016/j.scriptamat.2018.10.054.
[61] P. Luo, D.T. McDonald, W. Xu, S. Palanisamy, M.S. Dargusch, K. Xia, A modified hall–petch relationship in ultrafine-grained titanium recycled from chips by equal channel angular pressing, Scr. Mater. 66 (2012) 785–788, https://doi.org/10.1016/j.scriptamat.2012.02.008.
[62] J. Sun, Q. Yao, H. Xing, W.Y. Guo, Elastic properties of β, α″ and ω metastable phases in Ti–Nb alloy from first-principles, J. Phys. Condens. Matter 19 (2007) 486215, https://doi.org/10.1088/0953-8984/19/48/486215.
[63] A.Yu Eroshenko, YuP. Sharkeev, I.A. Glukhov, P.V. Uvarkin, A.M. Mairambekova, A.I. Tolmachev, The influence of dimesions and phase state of structural elements on mechanical properties of binary alloys of the Ti–Nb and Zr–Nb systems, Russ. Phys. J. 61 (2019) 1899–1907, https://doi.org/10.1007/s11182-019-01616-z.
[64] A. Thorvaldsen, The intercept method—2. Determination of spatial grain size, Acta Mater. 45 (1997) 595–600, https://doi.org/10.1016/S1359-6454(96)00198-X.
[65] S.-M. Chen, Z.-J. Ma, S. Qiu, L.-J. Zhang, S.-Z. Zhang, R. Yang, Q.-M. Hu, Phase decomposition and strengthening in HfNbTaTiZr high entropy alloy from first-principles calculations, Acta Mater. 225 (2022) 117582, https://doi.org/10.1016/j.actamat.2021.117582.
[66] A.J. Ardell, Precipitation hardening, Metall. Trans. A 16 (1985) 2131–2165, https://doi.org/10.1007/BF02670416.
[67] J. Wang, W. Xiao, Y. Fu, L. Ren, B. Song, C. Liu, C. Ma, Effects of initial microstructure on the aging behavior and subsequent mechanical properties of ti–nb–o titanium alloy, J. Mater. Res. 37 (2022) 2304–2313, https://doi.org/10.1557/s43578-022-00631-0.
[68] M. Tane, K. Hagihara, M. Ueda, T. Nakano, Y. Okuda, Elastic-modulus enhancement during room-temperature aging and its suppression in metastable Ti–Nb-based alloys with low body-centered cubic phase stability, Acta Mater. 102 (2016) 373–384, https://doi.org/10.1016/j.actamat.2015.09.030.
[69] S. Hanada, N. Masahashi, T.K. Jung, Effect of stress-induced α'' martensite on Young's modulus of β Ti–33.6Nb–4Sn alloy, Mater. Sci. Eng., A 588 (2013) 403–410, https://doi.org/10.1016/j.msea.2013.09.053.
[70] M. Niinomi, Mechanical properties of biomedical titanium alloys, Mater. Sci. Eng., A 243 (1998) 231–236, https://doi.org/10.1016/S0921-5093(97)00806-X.
[71] L.C. Zhang, D. Klemm, J. Eckert, Y.L. Hao, T.B. Sercombe, Manufacture by selective laser melting and mechanical behavior of a biomedical Ti–24Nb–4Zr–8Sn alloy, Scr. Mater. 65 (2011) 21–24, https://doi.org/10.1016/j.scriptamat.2011.03.024.
[72] S.L. Sing, W.Y. Yeong, F.E. Wiria, Selective laser melting of titanium alloy with 50 wt% tantalum: microstructure and mechanical properties, J. Alloys Compd. 660 (2016) 461–470, https://doi.org/10.1016/j.jallcom.2015.11.141.

[73] W. Chen, C. Chen, X. Zi, X. Cheng, X. Zhang, Y.C. Lin, K. Zhou, Controlling the microstructure and mechanical properties of a metastable β titanium alloy by selective laser melting, Mater. Sci. Eng., A 726 (2018) 240–250, https://doi.org/10.1016/j.msea.2018.04.087.
[74] R. Duan, S. Li, B. Cai, W. Zhu, F. Ren, M.M. Attallah, A high strength and low modulus metastable β Ti-12Mo-6Zr-2Fe alloy fabricated by laser powder bed fusion in-situ alloying, Addit. Manuf. 37 (2021) 101708, https://doi.org/10.1016/j.addma.2020.101708.
[75] J.C. Wang, Y.J. Liu, S.X. Liang, Y.S. Zhang, L.Q. Wang, T.B. Sercombe, L.C. Zhang, Comparison of microstructure and mechanical behavior of Ti-35Nb manufactured by laser powder bed fusion from elemental powder mixture and prealloyed powder, J. Mater. Sci. Technol. 105 (2022) 1–16, https://doi.org/10.1016/j.jmst.2021.07.021.
[76] H. Schaal, P. Castany, P. Laheurte, T. Gloriant, Design of a low Young's modulus Ti-Zr-Nb-Sn biocompatible alloy by in situ laser powder bed fusion additive manufacturing process, J. Alloys Compd. 966 (2023) 171539, https://doi.org/10.1016/j.jallcom.2023.171539.
[77] Z. Tang, G. Zhou, H. Xing, Z. Zhang, K. Lin, K. Zhang, J. RenXu, H. Zeng, Y. Yang, Tensile deformation behavior of Ti-Nb graded alloy fabricated by direct laser deposition, Adv. Light Mater. 1 (2026) 19–30, https://doi.org/10.1016/j.almate.2026.04.001.
[78] M. Tane, T. Ichitsubo, Effective-mean-field approach for macroscopic elastic constantsof composites, Appl. Phys. Lett. 85 (2004) 197–199, https://doi.org/10.1063/1.1769587.
[79] M. Tane, T. Ichitsubo, H. Nakajima, S.K. Hyun, M. Hirao, Elastic properties of lotus-type porous iron: acoustic measurement and extended effective-mean-field theory, Acta Mater. 52 (2004) 5195–5201, https://doi.org/10.1016/j.actamat.2004.07.030.
[80] M. Tane, Elastic properties of single-crystalline ω phase in titanium, Acta Mater. 61 (2013), https://doi.org/10.1016/j.actamat.2013.08.036.
[81] S. Higashino, D. Miyashita, T. Ishimoto, E. Miyoshi, T. Nakano, M. Tane, Low Young's modulus in laser powder bed fusion processed Ti–15Mo–5Zr–3Al alloys achieved by the control of crystallographic texture combined with the retention of low-stability bcc structure, Addit. Manuf. 102 (2025) 104720, https://doi.org/10.1016/j.addma.2025.104720.
[82] R.W. Messler, Principles of Welding, Wiley, New York, 2008.
[83] W. Liu, J.N. DuPont, Effects of melt-pool geometry on crystal growth and microstructure development in laser surface-melted superalloy single crystals: mathematical modeling of single-crystal growth in a melt pool (part I), Acta Mater. 52 (2004) 4833–4847, https://doi.org/10.1016/j.actamat.2004.06.041.
[84] K. Wang, D. Wu, D. Wang, Z. Deng, Y. Tian, L. Zhang, L. Liu, Influence of cooling rate on ω phase precipitation and deformation mechanism of a novel metastable β titanium alloy, Mater. Sci. Eng., A 829 (2022) 142151, https://doi.org/10.1016/j.msea.2021.142151.
[85] A. Devaraj, S. Nag, R. Srinivasan, R.E.A. Williams, S. Banerjee, R. Banerjee, H. L. Fraser, Experimental evidence of concurrent compositional and structural instabilities leading to ω precipitation in titanium–molybdenum alloys, Acta Mater. 60 (2012) 596–609, https://doi.org/10.1016/j.actamat.2011.10.008.
[86] M. Bönisch, A. Panigrahi, M. Calin, T. Waitz, M. Zehetbauer, W. Skrotzki, J. Eckert, Thermal stability and latent heat of Nb–rich martensitic Ti-Nb alloys, J. Alloys Compd. 697 (2017) 300–309, https://doi.org/10.1016/j.jallcom.2016.12.108.
[87] M.V. Pantawane, Y.-H. Ho, S.S. Joshi, N.B. Dahotre, Computational assessment of thermokinetics and associated microstructural evolution in laser powder bed fusion manufacturing of Ti6Al4V alloy, Sci. Rep. 10 (2020) 7579, https://doi.org/10.1038/s41598-020-63281-4.
[88] Y. Noyama, T. Miura, T. Ishimoto, T. Itaya, M. Niinomi, T. Nakano, Bone loss and reduced bone quality of the human femur after total hip arthroplasty under stress-shielding effects by titanium-based implant, Mater. Trans. 53 (2012) 565–570, https://doi.org/10.2320/matertrans.M2011358.
[89] A. Helth, S. Pilz, T. Kirsten, L. Giebeler, J. Freudenberger, M. Calin, J. Eckert, A. Gebert, Effect of thermomechanical processing on the mechanical biofunctionality of a low modulus Ti-40Nb alloy, J. Mech. Behav. Biomed. Mater. 65 (2017) 137–150, https://doi.org/10.1016/j.jmbbm.2016.08.017.
[90] W. Bonfield, M.D. Grynpas, Anisotropy of the Young's modulus of bone, Nature 270 (1977) 453–454, https://doi.org/10.1038/270453a0.